Research Square

Preprints are preliminary reports that have not undergone peer review.
They should not be considered conclusive, used to inform clinical practice,
or referenced by the media as validated information.

Neurodevelopmental disorder-associated Nr2f1 haploinsufficiency disrupts dentate gyrus inhibitory circuits and impairs short-term spatial memory

Eleonora Dallorto
University of Turin
Enis Hidisoglu
University of Turin
Sara Bonzano
University of Turin
Giuseppe Chiantia
University of Turin
Antonino Casile
Università di Camerino
Giulia Bonifazio
University of Turin
Annapaola Lippolis
University of Turin
Paolo Marcello Peretto
University of Turin
Marco Sassoè-Pognetto
University of Turin
Michèle Studer
Université Côte d'Azur
Andrea Marcantoni
University of Turin
Silvia De Marchis
silvia.demarchis@unito.it

University of Turin

Research Article

Keywords: NR2F1/COUP TF-1, Dentate Gyrus, Excitatory/inhibitory balance, GABAergic transmission, Neurodevelopmental disorders

Posted Date: October 30th, 2026

DOI: https://doi.org/10.21203/rs.3.rs-11281870/v1

License: This work is licensed under a Creative Commons Attribution 4.0 International License.
Read Full License

Additional Declarations: No competing interests reported.

Abstract

The dentate gyrus (DG) plays a central role in hippocampal information processing and spatial memory, functions that rely on a tightly regulated balance between excitation and inhibition, whose disruption is implicated in the pathophysiology of neurodevelopmental disorders.

Here, we used adult constitutive *Nr2f1* heterozygous knockout mice (*Nr2f1*$^{+/-}$) to investigate how *Nr2f1* haploinsufficiency affects DG inhibitory circuit organization and function in a model of Bosch-Boonstra-Schaaf optic atrophy syndrome (BBSOAS), a rare neurodevelopmental disorder associated with intellectual disability and learning impairment. *Nr2f1*$^{+/-}$ mice showed impaired short-term spatial memory associated with increased recruitment of mature dentate granule cells and a shift in the synaptic excitatory/inhibitory balance toward excitation in the DG. Reduced GABAergic synaptic input was accompanied by decreased presynaptic vGAT levels and a reduced density of parvalbumin positive interneurons. Electrophysiological analyses revealed a substantial reorganization of inhibitory signaling, with reduced phasic inhibition coexisting with enhanced asynchronous GABA release and increased THIP-evoked tonic currents. These findings show that *Nr2f1* haploinsufficiency differentially affects distinct modes of inhibition in the adult DG. Together, our results provide mechanistic insight into the cellular and synaptic alterations of DG inhibitory circuits that may contribute to cognitive impairment in BBSOAS with potential relevance to other neurodevelopmental disorders involving inhibitory circuit dysfunction.

INTRODUCTION

Cognitive impairment is a major clinical feature of neurodevelopmental disorders (NDDs), yet the neural circuit mechanisms linking disease-associated genes to altered cognitive function remain incompletely understood. The hippocampus is a key brain region involved in learning and memory, spatial navigation and emotions [1, 2], and its dysfunction has been associated with cognitive deficits across NDDs [3]. Within the hippocampus, the dentate gyrus (DG) serves as a critical gateway for information processing and memory encoding, functions that rely on a tightly regulated balance between excitation and inhibition. In the DG, inhibitory circuits are essential for maintaining sparse granule cell (GC) activity - a prerequisite for efficient pattern separation [4] - while altered excitatory/inhibitory (E/I) balance has emerged as a convergent mechanism in NDDs [5, 6]. Therefore, understanding how genetic alterations associated with NDDs affect these finely regulated circuits is crucial for defining the mechanisms underlying cognitive dysfunctions.

Bosch-Boonstra-Schaaf optic atrophy syndrome (BBSOAS; OMIM #615722 ORPHA:401777) is a rare, autosomal dominant monogenic NDD in which cognitive impairment represents a prominent clinical feature [7]. Since its initial description in 2014, BBSOAS has emerged as an increasingly diagnosed disorder, with an expanding number of reported cases worldwide and an estimated prevalence of 1 in 100,000-250,000 live births [8, 9]. The disorder is caused by pathogenic variants in the Nuclear Receptor subfamily 2, group f, member 1 gene (*NR2F1*), which encodes a highly evolutionarily conserved orphan

nuclear receptor, also known as chicken ovalbumin upstream promoter-transcription factor 1 (COUP-TF1). Reported pathogenic variants are mostly *de novo* and include gene deletions, translation initiation variants, INDELs and missense variants that result in loss-of-function or dominant-negative effects [8, 10]. Clinically, BBSOAS presents a broad phenotypic spectrum, characterized by developmental delay, intellectual disability (ID) and visual dysfunction [notably optic atrophy (OA) and cortical visual impairment (CVI)], frequently accompanied by hypotonia, epilepsy, speech difficulties and behavioral manifestations including autism spectrum disorder (ASD) and attention-deficit/hyperactivity disorder (ADHD) [8, 10].

Due to the similar expression patterns and the high amino-acid sequence identity (~ 98–100%) between human and mouse NR2F1, reflecting strong functional conservation [11, 12], mouse models represent a valuable tool for investigating BBSOAS. Previous studies using genetically modified mice, including *Nr2f1* conditional knockout (cKO) in pallial-derived glutamatergic neurons [13–16] or in subpallial-derived GABAergic neurons [17, 18], have established NR2F1 as a pleiotropic regulator of brain morphogenesis and cortical development controlling progenitor specification and proliferation, neuronal migration and differentiation in a stage- and context-dependent manner [14, 19–22]. Beyond its well-established role as a master regulator of neocortical development, including cortical patterning and laminar fate specification [14, 19, 23], increasing evidence highlights the involvement of NR2F1 in hippocampal development and function. During development, NR2F1 regulates hippocampal growth along the septo-temporal axis [15, 24] and controls the production and migration of dentate granule cells (GCs), thereby contributing to dentate gyrus (DG) morphogenesis [22]. Notably, GC generation in the DG continues throughout life [25, 26], and we previously demonstrated that NR2F1 regulates adult DG neural stem/progenitor cell fate decisions [27], as well as the survival and functional integration of adult-born neurons by shaping their mitochondrial network [28]. Despite this growing understanding of NR2F1 function in neural development, how reduced NR2F1 dosage alters mature hippocampal circuits and contributes to cognitive dysfunction remains largely unknown. MRI analyses have reported morphological hippocampal alterations in some BBSOAS patients [29], while recently developed mouse models carrying patient-specific *Nr2f1* variants or heterozygous deletions, consistent with the genetic condition observed in BBSOAS, show hippocampus-related morphological, functional and behavioral alterations [30, 31]. However, whether *Nr2f1* haploinsufficiency disrupts E/I balance and inhibitory circuit function in the adult DG, and whether these alterations are associated with cognitive impairment, has not been established.

In this study, we investigated the impact of *Nr2f1* haploinsufficiency on DG circuit function in adult mice using the constitutive heterozygous *Nr2f1*$^{+/-}$ mouse model, which recapitulates key features of BBSOAS [29, 32–34]. Integrating behavioral, cellular, molecular and electrophysiological approaches, we show that *Nr2f1* haploinsufficiency is associated with impaired DG-dependent short-term spatial memory, abnormal GC recruitment and a shift in synaptic E/I balance toward excitation. We further uncover an unexpected reorganization of inhibitory signaling, in which reduced phasic inhibition coexists with enhanced asynchronous GABA release and tonic inhibition, revealing a previously unrecognized form of DG inhibitory circuit dysfunction.

MATERIALS AND METHODS

Animals

All experiments were performed on adult (4- to 6-month-old) constitutive *Nr2f1* heterozygous KO mice (i.e. *Nr2f1*$^{wt/null}$, named *Nr2f1*$^{+/-}$), that were generated and genotyped as previously described [32]. Wild-type [*Nr2f1*$^{wt/wt}$ (WT)] littermates served as control. All mice were bred and maintained on a 129S2/SvP genetic background. Mice were housed under standard laboratory conditions (n = 2–6 mice/standard cage) with basic environmental enrichment under a 12 h light/dark cycle with food and water *ad libitum*. Both male and female mice were used in this study.

All procedures were conducted in accordance with the Guide for the Care and Use of Laboratory Animals of the European Community Council Directives (2010/63/EU and 86/609/EEC) and approved by institutional bioethics committee (OPBA), and the Italian Ministry of Health (Authorization number 49/2023-PR, protocol E6B5E.8), the institutional ethical committee (CIEPAL Azur 28 NCE/2024 – 976) and the Ministry for Higher Education and Research, France.

Behavioral analysis

Hippocampal-dependent spatial and short-term working memory were assessed with the Novel Object Location (NOL) [35, 36]. Male mice (WT: *n* = 11, *Nr2f1*$^{+/-}$: *n* = 7) were habituated in the testing room 30 min before the experiment. Both training and test sessions were performed in a small opaque plexiglass Phenotyper arena (50 cm x 33 cm x 33 cm; Noldus Information Technology). During the training session, each mouse was placed in the arena containing two identical objects positioned in parallel and allowed to explore for 10 minutes. After 1h inter-trial interval, the test session was performed in which one object was relocated to the opposite side of the arena to create a novel spatial configuration. Here, the mouse was allowed to explore the novel spatial configuration for 10 minutes. Behaviors were recorded using an overhead infrared camera and scored with BORIS (Behavioral Observation Research Interactive Software). Interaction time with the novel and familiar object locations was defined as the time spent sniffing the object. Behavioral events were annotated with time stamps, and data were exported for statistical analysis. Exploration preference was quantified using the Discrimination Index (DI), a standardized index of investigation. DI is calculated as $[(T_{novel} - T_{familiar}) / (T_{novel} + T_{familiar})]$, where T_{novel} and $T_{familiar}$ represent the time spent exploring the novel and familiar locations, respectively. The resulting score ranges from − 1 to + 1, when positive values indicate a higher level of investigation of the novel location. The interaction with the new object location can also be expressed as a function of the Recognition Index (RI): $[T_{novel} / (T_{novel} + T_{familiar})]$ [37, 38]. Moreover, Ethovision XT (Noldus Information Technology) software was used to track the locomotor activity, calculating total distance traveled and mean velocity to ensure no confounding motor deficits were present.

Tissue Preparation and Sectioning for Immunofluorescence Labelling

Adult mice were deeply anesthetized with a mixture of tiletamine and zolazepam (40–80 mg/kg Zoletil, Italy) and xylazine (4–5 mg/kg Rompun; Bayer, Wuppertal, Germany) by intraperitoneal injection (i.p.), and perfused transcardially with ice-cold 0.9% saline solution, followed by ice-cold 4% paraformaldehyde (PFA, Sigma-Aldrich 441244) in 0.1 M phosphate buffer (PB), pH 7.4. Then, brains were postfixed (2h), cryoprotected in a 30% sucrose solution (in 0.1 M PB pH 7.4) and embedded with cryo-embedding matrix (OCT; Killik, BioOptica), frozen, and stored at -80°C until cryostat cutting (Leica Mycrosystems). Free-floating 40 µm coronal serial sections were collected in series and subsequently stored at − 20°C in antifreeze solution (30% ethylene glycol, 30% glycerol, 10% PB: 189 mM NaH_2PO_4, 192.5 mM NaOH; pH 7.4) until use.

Immunofluorescence

Immunofluorescence reactions were performed on free-floating 40 µm-thick coronal serial sections as previously described [27, 28, 39]. Briefly, sections were incubated with primary antibodies (see Table 1) diluted in blocking solution [0.01 M PBS, pH 7.4, 1% Triton X-100 and 10% normal serum of the same species of the secondary antibody, i.e. normal donkey serum (NDS)] for 48 h at 4°C. Only for synaptic protein markers, sections underwent an additional permeabilization and blocking step prior to primary antibodies incubation. Specifically, slices were incubated for 1 hour in 1% Triton X-100 diluted in 0.01 M PBS (pH 7.4) for membrane permeabilization, followed by 45 minutes of blocking in a solution containing 1% Triton X-100 and 2% bovine serum albumin (BSA) in 0.01 M PBS (pH 7.4) at room temperature (RT). Sections were washed in PBS and incubated for 2 h with appropriate secondary antibodies (see Table 2) and 4,6-diamidino-2-phenylindole (DAPI; 1 µg/ml) to label nuclei in 0.01 M PBS (pH 7.4), 0.1% Triton X-100 and NDS (1%) at RT. Sections were then washed in 0.01 M PBS (pH 7.4) and mounted on gelatine-coated slides, air dried and coverslipped with antifade mounting medium Mowiol (4–88 reagent; 475904, Calbiochem).

Table 1
List of the primary antibodies

Primary Antibody	Host	Final dilution	Source	Use
anti-CTIP2	Rat	1:1000	Abcam, ab18465	Immunofluorescence
anti-c-Fos	Rabbit	1:10 000	Cell Signalling, 9F6#2250	Immunofluorescence
anti-DCX	Goat	1:2000	Santa Cruz, sc-8066	Immunofluorescence
anti-Gephyrin	Mouse	1:1600	Synaptic Systems, 147011	Immunofluorescence
anti-Parvalbumin	Mouse	1:2000	Swant, PV235	Immunofluorescence
Anti-Somatostatin, clone YC7	Rat	1:800	Sigma Aldrich - Millipore, MAB354	Immunofluorescence
anti-vGAT	Rabbit	1:2000 IF 1:1000 WB	Synaptic Systems, 131003	Immunofluorescence & Western Blot
anti-Vinculin	Mouse	1:2000	Sigma Aldrich, V9131	Western Blot

Table 2
List of the secondary antibodies

Secondary Antibody	Host	Final dilution	Source	Use
AlexaFluor488 Anti-Ck	Donkey	1:400	Jackson ImmunoResearch, 703-545-155	Immunofluorescence
AlexaFluor488 Anti-Ms	Donkey	1:400	Jackson ImmunoResearch, 715-545-151	Immunofluorescence
AlexaFluor594 Anti-Ms	Donkey	1:400	Jackson ImmunoResearch, 715-585-020	Immunofluorescence
AlexaFluor647 Anti-Rat	Donkey	1:600	Jackson ImmunoResearch, 712-605-153	Immunofluorescence
AlexaFluor647 Anti-Ms	Donkey	1:600	Jackson ImmunoResearch, 715-605-151	Immunofluorescence
Cy3 Anti-Rb	Donkey	1:800	Jackson ImmunoResearch, 711-165-152	Immunofluorescence
HRP Conjugated-anti-mouse	Goat	1:15.000	Cell Signalling, #7076	Western Blot
HRP Conjugated-anti-rabbit	Goat	1:15.000	Cell Signalling, #7074	Western Blot

Confocal Microscopy

Immunofluorescence images used for cell counting were acquired with TCS SP5 or Stellaris 5 confocal microscopes (Leica Microsystems). Confocal z-stacked images used for cell detection and counting analyses were captured through the thickness of the slice (40 µm) at 1-µm optical steps with an oil-immersed Plan-Apochromat 40X/1.25 objective, zoom 1.0, and resolution of 8 bit, 512/512 pixels and 400 Hz scan speed (1 pixel = 0.480µm) comprising both upper and lower blades of the hippocampal DG and corresponding molecular layers. Single-stack images of synaptic markers were acquired with LSM 910 (Zeiss) equipped with an Airyscan detector and processed using the Zeiss Airyscan automatic module, with an oil-immersed Plan-Apochromat 63X/1.4 objective, zoom 2.0, and resolution 8 bit, 1412x1412 pixels and 6 scan speed (1 pixel = 0.035 µm). For synaptic puncta, images were consistently acquired from a single optical plane located at the center of the slice thickness, and this setting was maintained for all slices and across all markers to ensure comparability. Importantly, all the parameters (i.e. laser power, gain, and offset) were kept constant across samples.

Microscope analysis and quantification

Cell quantification was performed on z-stacked confocal images using the ImageJ/Fiji Cell Counter plugin (https://imagej.net/plugins/cell-counter). cFos+ cells were manually counted throughout the entire DG granule cell layer (GCL), with DAPI staining used to trace the GCL boundaries. For each animal, at least three dorsal hippocampal slices along the rostrocaudal axis were included in the quantification to ensure representative sampling. Cell density was calculated by dividing the total number of counted cells over the area of interest and expressed as cells/mm^2. Slice cell density values were then averaged to obtain a single mean density value per animal.

For synaptic markers, fractional area (vGAT and gephyrin) was quantified via a semi-automated ImageJ workflow. Images underwent a pre-processing step that included first background subtraction (rolling ball radius: 50) and then Gaussian blur (sigma: 0.57). Subsequently, the vGAT or gephyrin channel was thresholded using the Default Dark algorithm (vGAT: 35–255, Gephyrin: 40–255). The resulting binary image was then cleaned outside the ROI to get the area occupied by synaptic protein staining within the selected ROI. Finally, we calculated the area fraction covered by vGAT and gephyrin on the selected ROI and expressed it as a percentage.

Puncta density, size, and juxtaposition were analysed with the SynBot Fiji macro [40] (https://github.com/Eroglu-Lab/Syn_Bot), maintaining the same pre-processing and thresholding parameters (see above). For the assessment of juxtaposition between vGAT and gephyrin puncta, we adopted the “pixel overlap colocalization” method rather than the circular approximation, as presynaptic vGAT-positive synaptic structures often deviate from canonical circular shapes. This approach allowed a more accurate estimation of the spatial overlap between inhibitory presynaptic and postsynaptic markers.

Hippocampal slice preparation

Acute hippocampal slices were prepared from 2- to 4-month-old *Nr2f1*$^{+/-}$ male mice and WT littermate controls (*n*: WT = 11 and *Nr2f1*$^{+/-}$=9) following deep anesthesia (as described above) and subsequent cervical dislocation. Brains were rapidly removed and placed in ice-cold sucrose-based cutting solution (Table 3) continuously oxygenated with 95% O_2 / 5% CO_2 (pH 7.3–7.4). Coronal hippocampal slices (300 µm) were obtained using a vibratome (Microm HM 650V, Thermo Scientific). Slices were then transferred to recording ACSF solution (Table 3) and allowed to recover for 30–45 min at 37°C, followed by an additional 1 h at RT before recordings.

Table 3
Composition of cutting solution, recording ACSF, and internal pipette solution used for electrophysiological recordings.

Component (mM)	Cutting Solution	Recording ACSF	Internal Solution
NaCl	—	119	—
KCl	2.5	2.5	—
NaH_2PO_4	1.25	1.2	—
$NaHCO_3$	26	26	—
$MgSO_4$	10	1.3	—
$CaCl_2$	0.5	2.5	—
Glucose	11	11	10
Sucrose	234	—	—
CsCl	—	—	90
TEA-Cl	—	—	20
EGTA	—	—	10
$MgCl_2$	—	—	1
ATP	—	—	4
GTP	—	—	0.5
Phosphocreatine	—	—	15

All concentrations are expressed in mM. "—" indicates absence of the component in the respective solution.

Solutions and toxins for electrophysiology

For spontaneous postsynaptic currents (sEPSC and sIPSCS) the patch electrodes were filled with the following solution (in mM): 130 K-gluconate, 10 KCl; 0.2 EGTA, 4 Mg-ATP, 10 HEPES, 0.3 Na2-GTP, 10 phosphocreatine di(tris), pH was adjusted to 7.2 with KOH. In order to block voltage-gated Na+ channels, QX-314 ((N-(2,6-dimethylphenyl carbamoylmethyl) triethylammonium bromide, 10 mM; Tocris) was added to the internal solution. During the recordings of miniature inhibitory postsynaptic currents (mIPSCs), the external ACSF solution was supplemented with DNQX (20 μM; Sigma-Aldrich), D-AP5 (50 μM; Sigma-Aldrich), and CGP 55845 (5 μM; Tocris) to block AMPA, NMDA, and $GABA_B$ receptors, respectively. The composition of the internal solution is shown in Table 3 (pH adjusted to 7.4 with CsOH) [41]. TTX (300 nM; Tocris) was also added to the external solution to block spontaneous action potentials propagation. Tonic currents were recorded in ACSF supplemented with TTX (300 nM), DNQX (20 μM), D-AP5 (50 μM) and CGP55845 (5 μM), and subsequently induced by bath application of THIP (1 μM, Gaboxadol hydrochloride (THIP) Sigma-Aldrich) to activate δ-subunit–containing $GABA_A$ receptors. For the recordings of evoked inhibitory postsynaptic currents (eIPSCs), slices were perfused at 1.2 mL/min with ACSF supplemented with DNQX (20 μM), D-AP5 (50 μM), and CGP58845 (5 μM) to block AMPA, NMDA, and $GABA_B$ receptors, respectively. eIPSCs were recorded with the same internal solution used for the mIPSCs. We also added QX-314 into the internal solution to block postsynaptic Na^+ currents activated during eIPSC recordings [41].

Patch clamp experiments

Patch electrodes (3–5 MΩ) were fabricated from thick-walled borosilicate glass. Whole-cell patch-clamp recordings were performed on DG granule neurons using a Multiclamp 700B amplifier (Molecular Devices). Only mature neurons with R_m< 300 MΩ were considered [42]. Spontaneous inhibitory (sIPSCs) and excitatory (sEPSCs) postsynaptic currents were recorded as previously described [43]. sEPSCs were recorded at a holding potential (Vh) of − 70 mV, corresponding to the chloride (Cl^-) electrochemical equilibrium potential calculated using the Nernst equation. Conversely, sIPSCs were recorded at a holding potential of + 10 mV, corresponding to the reversal potential of glutamatergic currents. The overall excitatory and inhibitory synaptic drive onto GCs was quantified by analyzing the amplitude, frequency, and cumulative charge transfer (total area) of spontaneous events recorded over a time interval of 30 s. Finally, the excitatory/inhibitory balance (E/I) was calculated as a measure of the relative contribution of excitatory and inhibitory synaptic inputs (Q_e/Q_i). GABAergic mIPSCs and eIPSCs were recorded at a holding potential of − 70 mV (Vh), sampled at 10 kHz, and low-pass filtered at 5 kHz using an eight-pole Bessel filter. Recordings with leak current > 100 pA or a series resistance > 20 MΩ were excluded. The mIPSC amplitude and frequency were analyzed using a 10 pA detection threshold. Single $GABA_A$ receptor current amplitude and average number of postsynaptic $GABA_A$ receptors activated by a quantum of neurotransmitter were estimated by non-stationary noise analysis of mIPSCs, as previously described [44]. Monosynaptic eIPSCs were evoked by extracellular stimulation of the medial perforant path by placing the monopolar glass electrode in the inner molecular layer of the suprapyramidal blade (filled with ACSF; intensity: 10–50 μA; pulse duration: 0.1 ms) connected to an isolated pulse stimulator (Model 2100; A-M Systems, Sequim). Monosynaptic eIPSCs were evoked at 0.1 Hz, and 15–20

consecutive responses were collected for analysis. Paired-pulse responses were obtained by recording eIPSCs elicited by two consecutive stimuli of increased interpulse intervals (from 25 to 150 ms), delivered every 10 s and paired-pulse depression (PPD) was calculated following the equation PPD = 100 × (A_1-A_2) / A_1. The size of the synchronous readily releasable pool (RRP_{syn}) and the probability that any given synaptic vesicle in the RRP_{syn} will be released (P_{ves}) were quantified using cumulative amplitude analysis [45]. RRP_{syn} was estimated from IPSCs evoked by a 40-pulse train at 20 Hz for 2 sec, assuming steady-state depression reflects a balance between vesicle release and recycling [46]. A linear fit of the steady-state phase was back-extrapolated to the y-axis to estimate the RRP_{syn} size, and P_{ves} was calculated as the ratio between the first eIPSC amplitude to the RRP_{syn}. Using a similar cumulative analysis, the size of total readily releasable pool (RRP_{tot}) represented by the number of synaptic vesicle available for synchronous and asynchronous release, was estimated by calculating the cumulative synaptic charge evoked by each stimulus during the train, after baseline offset subtraction, as previously described [41, 47–49]. Delayed asynchronous release was quantified following a 20 Hz, 2 s stimulus train by analyzing post-train currents over a 10 s window divided into 10 bins of 1 s duration. The charge transfer of each bin was calculated and normalized to the charge measured in the first 25 ms of the eIPSCs recorded 10 s before the train [50].

Synaptosomes isolation and Western Blot

Synaptosomes were isolated from fresh tissue of whole hippocampi of adult *Nr2f1*$^{+/-}$ and WT mice with the Syn-PER™ Synaptic Protein Extraction Reagent (87793, Thermo Fisher Scientific) supplemented with 1x protease inhibitor cocktail (Halt Protease Inhibitor Single-Use Cocktail 100X; 78430, Thermo Fisher Scientific), according to the manufacturer's instructions. Briefly, fresh hippocampi were isolated and washed twice with PBS supplemented with 0.6% glucose solution. Afterwards, pooled hippocampi were homogenized with a 2 ml Kimble dounce tissue grinder (D8938-1SET, Sigma-Aldrich) in the Syn-PER™ reagent and centrifuged (1200 g, 10 min, 4°C); the resulting supernatant was then transferred to a new tube and further centrifuged (15,000 g, 20 min, 4°C). Synaptosome pellets were resuspended in the same Syn-PER™ buffer and protein concentration was determined using a Bicinchoninic Acid (BCA) Protein Assay Kit (B9643, Sigma-Aldrich, Milan, Italy).

For Western Blot 20 µg of protein per sample was resolved on 4–20% precast polyacrylamide gel (Mini-PROTEAN® TGX Stain-Free; 4568096, Bio-Rad Laboratories), transferred to a supported nitrocellulose membrane (162 – 0093, Bio-Rad Laboratories) and blocked for 1 h at RT in 1× TBST (150 mM NaCl, 10 mM Tris-HCl pH 7.4, 0.1% Tween 20) containing 5% nonfat milk (1706404, Bio-Rad Laboratories). After blocking, the membrane was incubated overnight at 4°C with the primary antibodies (see Table 1), washed and incubated with the secondary horseradish peroxidase-linked antibodies (see Table 2). All primary antibodies were diluted in 1× TBST containing 5% bovine serum albumin (BSA) and 0.02% sodium azide, whereas all secondary antibodies were diluted in 1× TBST containing 5% nonfat milk. For protein band detection, the membrane was then incubated with a chemiluminescence substrate (Clarity Western ECL Substrate, 1705061; Clarity Max ECL Substrate, 1705062; Bio-Rad Laboratories). ECL

signals were detected with a ChemiDoc™ Imaging System, and bands were quantified using Image Lab version 6.1.0 build 7 software (2020, Bio-Rad Laboratories).

Statistics

Data are derived from at least three different animals/groups and are presented as mean ± SD, unless otherwise stated in the figure legends. Normal distribution was assessed with either the Shapiro-Wilk test (alpha, 0.05; if 3 < n < 50) or D'Agostino-Pearson (if n > 50). When comparing two populations of data, two-tailed unpaired Student's t-test was used to calculate statistical significance in cases of Gaussian distribution, applying Welch's correction in case of unequal variance distribution (F-test of equality of variances). Non-parametric Mann-Whitney' U-test was used in the case of non-Gaussian distribution. Kolmogorov-Smirnov test was carried out to compare cumulative distributions. In case of more than two sample groups normally distributed, one-way ANOVA followed by Tukey's test (parametric) or Kruskal-Wallis followed by Dunn's test (non-parametric) was performed. For immunofluorescence analysis of synaptic markers Nested t-test was used to ensure that statistical comparisons reflected variability between animals rather than within-animal sampling. Outliers were identified and excluded using Tukey's 1.5xIQR (Interquartile range) method (Fig. 1 and S1). Statistical significance was defined as follows: *P < 0.05, **P < 0.01 and ***P < 0.001. All analyses were performed using GraphPad Prism 8 software (GraphPad Software, San Diego, CA, USA).

RESULTS

Adult Nr2f1$^{+/-}$ Mice Show Impaired Short-term Spatial Memory

Given the contribution of the DG to spatial hippocampal memory processing [51, 52], we first assessed short-term spatial memory by employing the Novel Object Location (NOL) task (Fig. 1), which relies on the mouse innate tendency to preferentially explore novelty over familiarity [53–55]. Short-term spatial memory was assessed by measuring how long each mouse spent exploring the objects placed in familiar versus novel locations during the test phase (Fig. 1A, B). Wild-type (WT) mice spent significantly more time exploring (i.e. sniffing) the object placed in the novel location, whereas *Nr2f1*$^{+/-}$ mice did not show a preference for the displaced object (Fig. 1B). The discrimination index (DI, Fig. 1C,) showed positive values in WT mice but not in *Nr2f1*$^{+/-}$ animals. Similarly, the recognition index (RI), was significantly reduced in *Nr2f1*$^{+/-}$ mice, with mean values below 50%, indicating that mutant mice failed to preferentially explore the object in the novel location (Fig. 1D).

Although both genotypes spent comparable time interacting with the object in the familiar location (Fig. 1B), the overall interaction time was reduced in *Nr2f1*$^{+/-}$ mice (Fig. S1A). Importantly this reduction did not account for the impaired discrimination, as reflected by the decreased discrimination and recognition indices, which normalize for total exploration time. Moreover, the data on mobility duration (Fig. S1B) and total distance travelled during the test phase (Fig. S1C) did not differ significantly between

genotypes, indicating preserved locomotor activity. Overall, these findings indicate impaired short-term object location memory in *Nr2f1*$^{+/-}$ mice

Aberrant Activation of Mature DG Granule Neurons in Nr2f1$^{+/-}$ Mice

DG-dependent spatial memory relies on the sparse and selective activation of GC ensembles to encode novel spatial information [56]. Thus, impaired NOL performance (Fig. 1) suggests that *Nr2f1* haploinsufficiency may alter DG activity pattern. Aberrant activation of DG granule neurons has indeed been shown to affect short-term spatial memory by reducing pattern separation [57, 58]. To investigate whether DG neuronal recruitment is altered in *Nr2f1*$^{+/-}$ mice, we employed a “Novel Environment” (NE) paradigm, which induces sparse GC activation following short-term exploration (i.e. 30 minutes) of a novel environment. We focused on the dorsal DG and assessed the expression of the immediate early gene *Fos* (*cFos*), a widely used marker of activity-dependent neuronal activation [59, 60]. Following NE exposure *Nr2f1*$^{+/-}$ mice displayed a significant increase in cFos+ cells within the granule cell layer (GCL) compared to WT littermates (Fig. 2A, B). Analysis by GCL blade revealed a significant increase in cFos+ cell density in the upper blade, whereas the increase observed in the lower blade did not reach statistical significance (Fig. 2C). Overall, these findings demonstrate enhanced recruitment of granule neurons in the dorsal DG of adult *Nr2f1*$^{+/-}$ mice following NE exposure.

As the adult DG contains both mature GCs that have accumulated over time, and newborn immature neurons [26, 61, 62], we next sought to determine which GC population was preferentially recruited. Multiple immunostainings revealed that most cFos+ cells co-expressed CTIP2, consistent with a mature neuronal identity [63, 64] (Fig. 2D,D’,D”). In contrast, no colocalization was observed with doublecortin (DCX), a marker of immature newborn neurons [65] (Fig. 2D,D‴,D⁗). Together, these data suggest that *Nr2f1* haploinsufficiency leads to the abnormal activation of CTIP2 + mature granule neurons within the hippocampal DG circuit.

Reduced GABAergic inhibitory input onto DG granule neurons in Nr2f1$^{+/-}$ mice

To determine whether afferent synaptic inputs onto mature GCs were altered in *Nr2f1*$^{+/-}$ mice, we first analyzed spontaneous action potential-dependent excitatory (sEPSCs) (Fig. 3A-C) and inhibitory (sIPSCs) (Fig. 3D-F) postsynaptic currents in mature DG granule neurons in acute hippocampal slices from adult WT and *Nr2f1*$^{+/-}$ mice. We observed that the mean amplitude of sEPSCs recorded from WT GCs was not significantly different from that measured in *Nr2f1*$^{+/-}$ GCs (Fig. 3B, B’). Similarly, no significant difference was observed in the inter-event interval (IEI) of sEPSCs between WT and *Nr2f1*$^{+/-}$ GCs (Fig. 3C, C’). Consistent with these findings, the total excitatory charge transfer (Qe) was comparable between the two groups (Fig. 3G). Together, these results indicate that excitatory synaptic inputs onto GCs are largely preserved in *Nr2f1*$^{+/-}$ mice.

In contrast, the analysis of inhibitory synaptic inputs onto GCs revealed significant alterations. The mean sIPSCs amplitude was increased in *Nr2f1*$^{+/-}$ GCs compared with WT controls (Fig. 3E, E’). Moreover, the

IEI was also significantly increased (Fig. 3F, F'), indicating a lower frequency of inhibitory events. Overall, the total inhibitory charge transfer (Qi) was significantly reduced in *Nr2f1*$^{+/-}$ GCs compared with WT GCs (Fig. 3H). To assess the balance between excitatory and inhibitory synaptic inputs, we compared the Qe/Qi ratio between genotypes and found a significant increase in *Nr2f1*$^{+/-}$ GCs (Fig. 3I), indicating a shift toward a relative predominance of excitatory over inhibitory synaptic drive. Collectively, these findings suggest that in *Nr2f1*$^{+/-}$ mice, inhibitory afferent input onto GCs is reduced, whereas excitatory synaptic transmission remains largely unaffected.

We therefore focused on GABAergic synapses and measured miniature inhibitory postsynaptic currents (mIPSCs) in mature DG granule neurons (Fig. 3J), to evaluate quantal inhibitory synaptic transmission independently of network activity.

No differences between WT and *Nr2f1*$^{+/-}$ GCs were detected when mIPSCs amplitude, single $GABA_A$ channel current or number of postsynaptic $GABA_A$ receptors activated by single quanta of neurotransmitter were considered (Fig. 3K, K'; Fig. S2A, B). In contrast, *Nr2f1*$^{+/-}$ GCs exhibited significantly longer mIPSCs IEI (Fig. 3L, L'). Overall, these findings support reduced inhibitory synaptic input onto *Nr2f1*$^{+/-}$ GCs. The reduced frequency of mIPSCs, together with their unchanged amplitude, is consistent with fewer functional GABAergic synapses and/or a reduced rate of GABA release at the presynaptic site, rather than altered postsynaptic $GABA_A$ receptor function.

We next examined GABAergic terminals by quantifying the expression of the presynaptic vesicular GABA transporter (vGAT) [66]. Western blot analysis of synaptosome protein extracts from adult hippocampi revealed significantly reduced vGAT levels in *Nr2f1*$^{+/-}$ mice compared to WT controls (Fig. 4A-C), which is consistent with the increased mIPSCs IEI (Fig. 3L, L'). To examine presynaptic sites at subcellular level, we performed immunofluorescence combined with high-resolution confocal microscopy quantifying vGAT+ puncta in the GCL and inner molecular layer (iMCL) of the DG (Fig. 4D). This approach allows the selective assessment of somatic (GCL) and proximal dendritic (iMCL) inhibitory inputs. Fractional area analysis revealed a significant reduction in vGAT immunoreactivity in both the iMCL (~23%) and the GCL (~17% decrease) (Fig. 4D, E, H) in *Nr2f1*$^{+/-}$ mice. We next employed the SynBot Fiji macro [40] to segment and analyse individual vGAT+ puncta with consistent threshold parameters. We found a significant reduction in vGAT+ puncta size, as indicated by a leftward shift in the cumulative distribution of puncta areas, and a reduction in the mean puncta area in *Nr2f1*$^{+/-}$ mice (Fig. 4F, I). However, vGAT+ puncta density did not differ between genotypes (Fig. S2 C, D). Furthermore, the fraction of vGAT+ puncta juxtaposed to gephyrin - a postsynaptic inhibitory scaffold protein [67] - remained unchanged (Fig. 4G, J), which is consistent with preserved postsynaptic receptor function (Fig. 3K). Taken together, these findings identify a presynaptic GABAergic deficit in the adult *Nr2f1*$^{+/-}$ DG.

To determine whether these presynaptic alterations were associated with changes in DG interneuron composition, we quantified the parvalbumin (PV) and somatostatin (SST) immunopositive cells in the DG, representing the two major classes of hippocampal GABAergic interneurons [68–70]. Adult *Nr2f1*$^{+/}$

⁻mice showed a significant reduction in the PV+ interneuron population (~38.3%) compared with WT controls (Fig. 4K, L), whereas the STT+ interneuron population did not differ significantly (Fig. 4M, N). Given the well-established role of PV+ interneurons in regulating GC spiking through lateral inhibition and promoting sparse coding [70, 71], their reduction is likely to contribute to the impaired inhibitory control observed in Nr*2f1*$^{+/-}$ mice.

GABAergic terminals in Nr2f1$^{+/-}$ mice exhibit enhanced asynchronous neurotransmitter release

The reduced frequency of mIPSCs observed in *Nr2f1*$^{+/-}$ GCs suggested a presynaptic impairment at GABAergic synapses onto GCs. To further investigate presynaptic functions, we performed whole-cell voltage-clamp recordings from GCs while applying extracellular stimulation of the medial perforant pathway to induce monosynaptic eIPSCs [42, 72]. Paired-pulse stimulation of the DG in WT and *Nr2f1*$^{+/-}$ mice [73] (Fig. S3A, B) revealed no differences between the two genotypes in the degree of paired-pulse depression (PPD) (Fig. S3A', B'), suggesting that basal presynaptic release probability and short-term synaptic plasticity were preserved. However, during sustained high-frequency stimulation (20Hz for 2 sec) [41, 49] a distinct phenotype emerged (Fig. 5A). In WT neurons, the eIPSCs amplitude was maximal during the first pulse of the train and progressively decreased, reaching a steady-state level during the final 7–8 pulses, consistent with synaptic depression (Fig. 5B). While the average eIPSC amplitude, determined by synchronous release, was comparable between WT and *Nr2f1*$^{+/-}$ neurons, the area underlying the train, reflecting asynchronous release, was significantly increased in *Nr2f1*$^{+/-}$ GCs (Fig. 5A). This observation was confirmed by the similar distribution of normalized eIPSCs amplitude between the two genotypes (Fig. 5B), and the significantly increased normalized distribution of eIPSCs area in *Nr2f1*$^{+/-}$ neurons (Fig. 5H). Moreover, analysis of the cumulative distribution of eIPSCs amplitudes demonstrated that neither the size of the synchronous readily releasable pool (RRP_{syn}), nor the probability that any given synaptic vesicle in the RRP_{syn} will be released (P_{ves}) differed between genotypes (Fig. 5D, E). In contrast, analysis of cumulative eIPSC area during 20Hz stimulation (Fig. 5F) revealed a significant increase of the total readily releasable pool (RRP_{TOT}) size in *Nr2f1*$^{+/-}$ neurons (Fig. 5G). Since the size of the RRP_{syn} was unchanged (Fig. 5D), the increase in RRP_{TOT} was attributed to an expansion of the asynchronous readily releasable pool (RRP_{asyn}) size in *Nr2f1*$^{+/-}$ neurons. Consistently the amount of delayed asynchronous GABA release was significantly enhanced in *Nr2f1*$^{+/-}$ neurons during the 1 s after the end of the stimulus (Fig. 5I-K). Overall, our findings suggest that the inhibitory synapses on *Nr2f1*$^{+/-}$ DG granule neurons are characterized by a presynaptic increase of asynchronous (Fig. 5A, H) and delayed asynchronous release of GABA (Fig. 5I-K) sustained by the increased size of RRP_{asyn}.

Enhanced tonic GABAergic inhibition in Nr2f1$^{+/-}$ DG granule neurons

Given the enhanced asynchronous release observed in *Nr2f1*$^{+/-}$ DG (Fig. 5H-K), we next asked whether this increased inhibitory charge could reshape postsynaptic inhibitory organization at the perisomatic

region of the GCs. We therefore examined the distribution of $GABA_A$ receptor scaffolding protein gephyrin within the GCL. Immunofluorescence analysis revealed increased gephyrin signal across DG layers in *Nr2f1*$^{+/-}$ mice compared to WT controls (Fig. 4D, Fig. 6A). Quantification of the area fraction covered by gephyrin immunoreactivity in the GCL demonstrated a significant increase (~47% increase) in *Nr2f1*$^{+/-}$ mice (Fig. 6B). Using identical thresholding parameters previously applied to generate gephyrin masks for occupancy analysis, we segmented individual gephyrin-positive puncta and quantified their properties within the GCL. Cumulative distribution analysis revealed a rightward shift in puncta area in *Nr2f1*$^{+/-}$ mice, indicating a significant enlargement of gephyrin clusters (Fig. 6C).

We also observed a significant increase in gephyrin puncta density (~47%) in *Nr2f1*$^{+/-}$ mice (Fig. 6D), indicating increased postsynaptic gephyrin scaffolding in GCs. Quantification of GABAergic synaptic contacts, defined as gephyrin-positive puncta juxtaposed with the presynaptic marker vGAT (i.e. % juxtaposed GABAergic puncta/gephyrin puncta), revealed a significant reduction in synaptic gephyrin clusters (~10% decrease) (Fig. 6E). Conversely, the proportion of non-juxtaposed (“extrasynaptic”) gephyrin puncta was significantly increased (~28% increase) (Fig. 6F). These findings suggest a redistribution of gephyrin away from synaptic sites and toward extrasynaptic compartments, consistent with an expansion of the extrasynaptic $GABA_A$ receptor pool. To functionally test this hypothesis, we performed patch-clamp recordings on DG granule neurons and quantified the average amplitude of GABAergic current activated by 1 μM THIP, a preferential agonist of δ-subunit-containing $GABA_A$ receptors that mediate extrasynaptic tonic inhibition in DG granule cells. In line with the immunofluorescence data, we observed that THIP induced significantly larger tonic current in *Nr2f1*$^{+/-}$ mice compared to WT controls (Fig. 6G, H), indicating enhanced extrasynaptic GABAergic conductance. Together, these results reveal a shift from synaptic to extrasynaptic GABAergic inhibition in *Nr2f1*$^{+/-}$ DG granule cells, leading to increased tonic inhibition.

DISCUSSION

Understanding how neurodevelopmental disorder-associated genes affect circuit function beyond development is critical for defining the mechanisms underlying cognitive impairment. Here, we identify the DG as a key site of circuit dysfunction in adult *Nr2f1* haploinsufficient mice, with impaired short-term spatial memory associated with abnormal recruitment of mature GCs and a shift in synaptic E/I balance toward excitation. Importantly, our findings reveal a substantial reorganization of inhibitory signaling, in which reduced phasic inhibition coexists with enhanced asynchronous GABA release and increased tonic inhibition. Together, these findings provide mechanistic insight into how *Nr2f1* haploinsufficiency alters adult DG circuit function. This is particularly relevant to BBSOAS, in which intellectual disability and learning difficulties are prominent clinical features [8, 10]. The DG plays a critical role in sparse coding and pattern separation, processes required for memory formation, spatial navigation, novelty detection, and fine spatial discrimination [74–76]. Thus, the alterations identified here provide a plausible circuit substrate for cognitive dysfunction associated with *NR2F1* deficiency.

DG-dependent short-term spatial memory deficits and altered exploratory behavior

Nr2f1 $^{+/-}$ mice displayed impaired performance in a DG-dependent short-term memory task. This deficit cannot be attributed to altered locomotor activity as mobility duration and distance travelled were unchanged. Although total object interaction time was reduced, interaction with the object in the familiar location was comparable to WT controls, suggesting preserved task-directed behavior. Moreover, the reduced interaction with the displaced object emerged in both the discrimination and the recognition indices, which normalize for total exploration time, indicating a specific deficit in spatial memory processing. However, we cannot exclude that altered motivation or exploratory drive could contribute to the reduced exploration of the displaced object. Reduced exploratory behavior has previously been reported in mouse models relevant to ASD [77–79], and may represent an additional behavioral feature associated with Nr2f1 haploinsufficiency, consistent with recent observations in patient-variant BBSOAS models [31].

DG inhibitory circuit dysfunction and aberrant granule cell recruitment

DG-dependent spatial memory relies on the sparse and selective activation of GC ensembles, a process critically shaped by local inhibitory circuits and essential for effective pattern separation [4]. Following brief exposure to a novel environment, we observed a significant increase in cFos+ mature GCs in the DG of *Nr2f1*$^{+/-}$ mice, indicating enhanced activation of granule neurons in response to novelty. This increased activation is consistent with a reduction in the sparse coding properties of the DG. Accordingly, excessive recruitment of GCs has been associated with impaired pattern separation and deficits in DG-dependent memory tasks [57, 58]. Thus, the aberrant activation of mature GCs observed in *Nr2f1*$^{+/-}$ mice likely contributes to their impaired short-term spatial memory. GC activity is primarily regulated by excitatory inputs from the perforant path and by local GABAergic interneurons [71, 75, 80, 81]. Our electrophysiological data indicate that in the *Nr2f1*$^{+/-}$ DG, inhibitory synaptic input onto GCs is reduced when compared to excitatory input, resulting in an altered E/I balance that favors the excitatory synaptic drive. Indeed, sIPSCs and mIPSCs analyses revealed a reduced frequency of inhibitory events in *Nr2f1*$^{+/-}$ GCs, whereas sEPSC remained unaffected. The reduction in inhibitory input was further supported by decreased vGAT protein levels in hippocampal synaptosomes and reduced vGAT immunoreactivity throughout the DG, pointing to a presynaptic GABAergic deficit.

Among interneuron subtypes shaping DG activity, PV interneurons provide strong perisomatic inhibition of dentate GCs, preventing overexcitation, maintaining circuit stability and supporting pattern separation [71, 82, 83]. Accordingly, depletion of PV interneurons has been associated with impaired network function and cognitive deficits [84, 85]. We found a significant reduction in PV+ interneurons in the DG of *Nr2f1*$^{+/-}$ mice. This observation is consistent with the decreased mIPSC frequency and lower vGAT expression observed in *Nr2f1*$^{+/-}$ mice, supporting the idea that impaired PV-mediated inhibition

contributes to the DG inhibitory phenotype. These findings also align with the well-established role of NR2F1 in inhibitory circuit development, where it regulates the specification, migration and subtype composition of GABAergic interneurons, thus contributing to the assembly of functional inhibitory networks in the mature brain [17, 18, 86, 87]. Collectively, these findings support a model in which developmental alterations driven by *Nr2f1* haploinsufficiency have lasting consequences for the organization and function of inhibitory circuits within the adult DG.

Notably, despite the overall reduction in inhibitory input onto GCs, sIPSCs in *Nr2f1*$^{+/-}$ mice exhibited not only a reduced frequency but also an increased amplitude. In contrast, mIPSC and eIPSC amplitudes were unchanged between genotypes. Because mIPSCs were recorded in the presence of TTX, the unchanged mIPSC amplitudes indicate that quantal inhibitory transmission and basal postsynaptic $GABA_A$ receptor function are largely preserved. Likewise, comparable eIPSC amplitudes indicate that the inhibitory response evoked by individual presynaptic action potentials remains largely intact. These findings suggest that the increase in sIPSC amplitude arises from alterations in action potential-dependent inhibitory network activity, possibly involving changes in the excitability, firing patterns, or synchronization of GABAergic interneurons.

Importantly, our findings establish a link between *Nr2f1* haploinsufficiency and altered E/I balance and GABAergic circuit dysfunction, mechanisms broadly implicated in NDDs [5, 6]. This is particularly relevant to ASD, as *NR2F1* is recognized by SFARI as a strong ASD candidate gene and ASD-related behavioral alterations, including deficits in social communication, have recently been reported in *Nr2f1*$^{+/-}$ mice [31]. GABAergic circuit dysfunction is also strongly implicated in epilepsy [6], another frequent clinical feature of BBSOAS [8, 10, 88].

Enhanced asynchronous GABA release and tonic inhibition in the DG

Despite the reduced number of inhibitory synaptic contacts onto *Nr2f1*$^{+/-}$ GCs, the functional properties of the inhibitory synapses during synchronous release, which is mainly mediated by PV interneurons [89], remained comparable to those observed in WT mice. Interestingly, high-frequency stimulation revealed a selective enhancement of asynchronous and delayed asynchronous GABA release in *Nr2f1*$^{+/-}$ DG, a form of inhibition that in the DG is primarily driven by CCK interneurons [89]. Since the size of RRP_{syn} measured in *Nr2f1*$^{+/-}$ was unchanged despite an increase in the RRP_{tot}, our data support a selective increase of the RRP_{asyn} in these mice, which is likely to underlie the potentiation of asynchronous and delayed asynchronous release.

Asynchronous release is driven by an increase in bulk cytosolic Ca^{2+} during repetitive activity and primarily involves vesicles that are already docked and primed within the RRP_{asyn} but remain reluctant to fuse, either because of their intrinsically lower sensitivity to intracellular Ca^{2+} and slower fusion kinetics, or because they are located farther from presynaptic Ca^{2+} channels [90–94]. Following stimulus termination, delayed asynchronous release reflects the continued fusion of these slowly releasing

vesicles, and may also involve rapid recruitment of additional vesicles from recycling and deeper reserve/resting pools [91, 92, 95, 96]. The enhancement of asynchronous release observed in *Nr2f1*$^{+/-}$ mice suggests a possible defect in bulk Ca^{2+} clearance or buffering mechanisms whose functional consequences become evident during sustained neuronal activity. Among the mechanisms regulating presynaptic Ca^{2+} dynamics, mitochondrial Ca^{2+} buffering is a major determinant of asynchronous neurotransmitter release, as mitochondrial Ca^{2+} uptake during high-frequency stimulation limits the accumulation of residual Ca^{2+} [91]. Although the mechanisms underlying the enhanced asynchronous release remain to be established, these observations are consistent with the possibility that impaired mitochondrial function may influence Ca^{2+} dynamics and contribute to the electrophysiological phenotype observed in *Nr2f1*$^{+/-}$ mice.

Enhanced asynchronous release is expected to increase extracellular GABA availability and spillover, thereby preferentially engaging extrasynaptic $GABA_A$ receptors and strengthening tonic inhibition [72]. Consistent with this model, *Nr2f1*$^{+/-}$ mice exhibited an increased density of gephyrin+ puncta together with a redistribution of gephyrin away from vGAT+ synaptic terminals. Although gephyrin is primarily associated with synaptic $GABA_A$ receptors, under developmental, plasticity, or pathological conditions, it can redistribute and cluster inhibitory receptors at extrasynaptic sites [67, 97, 98]. Our findings therefore suggest a redistribution of gephyrin towards extrasynaptic compartments, consistent with an expansion of the extrasynaptic $GABA_A$ receptor pool. Accordingly, activation of δ-subunit-containing extrasynaptic $GABA_A$ receptors with THIP evoked a significantly larger tonic current in *Nr2f1*$^{+/-}$ GCs, demonstrating enhanced extrasynaptic inhibitory conductance. Although increased tonic inhibition is generally expected to dampen neuronal excitability, its functional consequences are likely to depend on its interaction with the concomitant reduction in phasic inhibition found in the *Nr2f1*$^{+/-}$ DG. Whether the observed pattern of inhibitory signaling represents a compensatory adaptation to reduced synaptic inhibition or a maladaptive circuit response remains to be established. Nevertheless, this remodeling is likely to alter the temporal regulation of GC activity, and interfere with sparse coding, providing a plausible circuit mechanism for the DG-dependent memory deficits observed in *Nr2f1*$^{+/-}$ mice.

CONCLUSIONS

Our study identifies the DG as a key site of circuit dysfunction in adult Nr2f1 haploinsufficient mice. By uncovering alterations in synaptic E/I balance and inhibitory signaling associated with aberrant GC recruitment and impaired DG-dependent memory, our findings provide new insight into the circuit mechanisms that may contribute to cognitive dysfunction in BBSOAS, with potential relevance to other NDD involving inhibitory circuit dysfunction.

Abbreviations

ADHD: Attention-deficit/hyperactivity disorder

ASD: Autism spectrum disorder

BBSOAS: Bosch-Boonstra-Schaaf optic atrophy syndrome

BSA: Bovine serum albumin

CCK: Cholecystokinin (interneurons)

c-Fos: Fos (immediate early gene)

cKO: Conditional knockout

COUP-TF1: Chicken ovalbumin upstream promoter-transcription factor 1

CTIP2: COUP-TFII-interacting protein 2

CVI: Cortical visual impairment

DAPI: 4',6-diamidino-2-phenylindole

DCX: Doublecortin

DG: Dentate gyrus

DI: Discrimination Index

DNQX: 6-cyano-7-nitroquinoxaline-2,3-dione

D-AP5: D(-)-2-amino-5-phosphonopentanoic acid

E/I: Excitatory/inhibitory

eIPSC: Evoked inhibitory postsynaptic current

EGTA: Ethylene glycol-bis(beta-aminoethyl ether)-N,N,N',N'-tetraacetic acid

GC: Granule cell

GCL: Granule cell layer

HEPES: 4-(2-hydroxyethyl)-1-piperazineethanesulfonic acid

ID: Intellectual disability

IEI: Inter-event interval

iMCL: Inner molecular layer

KO: Knockout

mIPSC: Miniature inhibitory postsynaptic current

MRI: Magnetic resonance imaging

NDD: Neurodevelopmental disorder

NDS: Normal donkey serum

NOL: Novel Object Location (test)

NR2F1: Nuclear Receptor subfamily 2, group f, member 1

OA: Optic atrophy

OCT: Optimal cutting temperature

PB: Phosphate buffer

PBS: Phosphate-buffered saline

PFA: Paraformaldehyde

PPD: Paired-pulse depression

PSD: Postsynaptic density

Pves: Vesicle release probability

PV: Parvalbumin

Qi: Inhibitory charge transfer

Qe: Excitatory charge transfer

QX-314: (N-(2,6-dimethylphenyl carbamoylmethyl) triethylammonium bromide)

RI: Recognition Index

RRP: Readily releasable pool

RRPasyn: Asynchronous readily releasable pool

RRPsyn: Synchronous readily releasable pool

RRPTOT: Total readily releasable pool

RT: Room temperature

SD: Standard deviation

sEPSC: Spontaneous excitatory postsynaptic current

sIPSC: Spontaneous inhibitory postsynaptic current

SST: Somatostatin

THIP: Gaboxadol hydrochloride (4,5,6,7-tetrahydroisoxazolo[5,4-c]pyridin-3-ol)

TTX: Tetrodotoxin

vGAT: Vesicular GABA transporter

Vh: Holding potential

WT: Wild-type

Declarations

Ethics approval and consent to participate

All procedures were conducted in accordance with the Guide for the Care and Use of Laboratory Animals of the European Community Council Directives (2010/63/EU and 86/609/EEC) and approved by institutional bioethics committee (OPBA), and the Italian Ministry of Health (Authorization number 49/2023-PR, protocol E6B5E.8), the institutional ethical committee (CIEPAL Azur 28 NCE/2024-976) and the Ministry for Higher Education and Research, France.

Consent for publication

Not applicable

Availability of data and material

All data generated or analyzed during this study are included in this published article (and its supplementary information files). SynBot analysis macros are publicly available at https://github.com/Eroglu-Lab/Syn_Bot .

Conflict of Interest

The authors declare no competing or financial interests.

Fundings

This work is supported by PRIN 2022 Prot. 2022WJFN5X and a grant from the NR2F1 Foundation to SDM; PRIN PNRR MUR 2022 Prot. P2022CRAXJ to AM; Fondazione Cassa di Risparmio di Torino (CRT) 2024/0438 to SB; Fondation pour la Recherche sur le Cerveau (FRC 2025) to M.S. ED was a recipient of a PhD fellowship from the Vinci Program Cap III (C3-2226) of the “Italian-French University” (UIF) under SDM and MS co-tutoring and currently holds a Research Position (Incarico di Ricerca) funded by the NR2F1 Foundation.

Authors' contributions

Conceptualization: E.D., E.H., S.B, A.M., S.D.M.; Validation: E.D., E.H., A.M., S.D.M.; Formal analysis: E.D., E.H., S.B, G.C., A.C., G.B., A.L.; Investigation E.D., E.H., S.B., G.C., A.C., G.B.; Resources: P.P., M.S-P., M.S.; Data curation: E.D., E.H., S.B., G.C..; Writing - original draft: E.D., E.H., A.M., S.D.M.; Writing - review & editing: E.D., E.H., S.B., G.C., P.P, M.S-P., M.S., A.M., S.D.M.; Visualization: E.D., E.H., S.B., G.C.; Supervision: A.M., S.D.M.; Project administration: S.D.M.; Funding acquisition: S.B., M.S, A.M., S.D.M.

Acknowledgements

We thank Riccardo Pizzo for assistance with confocal imaging of synapses and Stefano Zucca for helpful discussions, and all members of the Laboratory of Adult Neuroplasticity at NICO for their support.

References

1. Anand KS, Dhikav V (2012) Hippocampus in health and disease: An overview. Ann Indian Acad Neurol 15:239–246
2. Rolls ET (2023) The hippocampus, memory, and spatial function. In: Rolls ET (ed) Brain Computations and Connectivity. Oxford University Press, p 0
3. Li Y, Shen M, Stockton ME, Zhao X (2019) Hippocampal deficits in neurodevelopmental disorders. Neurobiol Learn Mem 165:106945
4. Hainmueller T, Bartos M (2020) Dentate gyrus circuits for encoding, retrieval and discrimination of episodic memories. Nat Rev Neurosci 21:153–168
5. Tang X, Jaenisch R, Sur M (2021) The role of GABAergic signalling in neurodevelopmental disorders. Nat Rev Neurosci 22:290–307
6. Bozzi Y, Provenzano G, Casarosa S (2018) Neurobiological bases of autism–epilepsy comorbidity: a focus on excitation/inhibition imbalance. Eur J Neurosci 47:534–548
7. Bosch DGM, Boonstra FN, Gonzaga-Jauregui C, Xu M, de Ligt J, Jhangiani S et al (2014) NR2F1 Mutations Cause Optic Atrophy with Intellectual Disability. Am J Hum Genet 94:303–309
8. Bertacchi M, Tocco C, Schaaf CP, Studer M (2022) Pathophysiological Heterogeneity of the BBSOA Neurodevelopmental Syndrome. Cells 11:1260

9. Gillentine MA, Wang T, Eichler EE (2022) Estimating the Prevalence of De Novo Monogenic Neurodevelopmental Disorders from Large Cohort Studies. Biomedicines 10:2865
10. Chen C-A, Bosch DGM, Cho MT, Rosenfeld JA, Shinawi M, Lewis RA et al (2016) The expanding clinical phenotype of Bosch-Boonstra-Schaaf optic atrophy syndrome: 20 new cases and possible genotype–phenotype correlations. Genet Med 18:1143–1150
11. Qiu Y, Krishnan V, Zeng Z, Gilbert DJ, Copeland NG, Gibson L et al (1995) Isolation, characterization, and chromosomal localization of mouse and human COUP-TF I and II genes. Genomics 29:240–246
12. Alfano C, Studer M (2013) Neocortical arealization: evolution, mechanisms, and open questions. Dev Neurobiol 73:411–447
13. Alfano C, Viola L, Heng JI-T, Pirozzi M, Clarkson M, Flore G et al (2011) COUP-TFI promotes radial migration and proper morphology of callosal projection neurons by repressing Rnd2 expression. Development 138:4685–4697
14. Alfano C, Magrinelli E, Harb K, Hevner RF, Studer M (2014) Postmitotic control of sensory area specification during neocortical development. Nat Commun 5:5632
15. Flore G, Di Ruberto G, Parisot J, Sannino S, Russo F, Illingworth EA et al (2017) Gradient COUP-TFI Expression Is Required for Functional Organization of the Hippocampal Septo-Temporal Longitudinal Axis. Cereb Cortex 27:1629–1643
16. Feng J, Hsu W-H, Patterson D, Tseng C-S, Hsing H-W, Zhuang Z-H et al (2021) COUP-TFI specifies the medial entorhinal cortex identity and induces differential cell adhesion to determine the integrity of its boundary with neocortex. Sci Adv 7:eabf6808
17. Lodato S, Tomassy GS, Leonibus ED, Uzcategui YG, Andolfi G, Armentano M et al (2011) Loss of COUP-TFI Alters the Balance between Caudal Ganglionic Eminence- and Medial Ganglionic Eminence-Derived Cortical Interneurons and Results in Resistance to Epilepsy. J Neurosci 31:4650–4662
18. Touzot A, Ruiz-Reig N, Vitalis T, Studer M (2016) Molecular control of two novel migratory paths for CGE-derived interneurons in the developing mouse brain. Development 143:1753–1765
19. Tomassy GS, De Leonibus E, Jabaudon D, Lodato S, Alfano C, Mele A et al (2010) Area-specific temporal control of corticospinal motor neuron differentiation by COUP-TFI. Proc Natl Acad Sci U S A 107:3576–3581
20. Alfano C, Magrinelli E, Harb K, Studer M (2013) The nuclear receptors COUP-TF: a long-lasting experience in forebrain assembly. Cell Mol Life Sci 71:43–62
21. Bovetti S, Bonzano S, Garzotto D, Giannelli SG, Iannielli A, Armentano M et al (2013) COUP-TFI controls activity-dependent tyrosine hydroxylase expression in adult dopaminergic olfactory bulb interneurons. Development 140:4850–4859
22. Parisot J, Flore G, Bertacchi M, Studer M (2017) COUP-TFI mitotically regulates production and migration of dentate granule cells and modulates hippocampal Cxcr4 expression. Development 144:2045–2058

23. Zhou C, Qiu Y, Pereira FA, Crair MC, Tsai SY, Tsai MJ (1999) The nuclear orphan receptor COUP-TFI is required for differentiation of subplate neurons and guidance of thalamocortical axons. Neuron 24:847–859
24. Tseng C-S, Zhuang Z, Hsing H-W, Lee C-M, Hsu T-T, Pan Y-K et al (2025) A developmental gradient of COUP-TFI expression regulates the relative size of hippocampus dorsal and ventral subregions. PLoS Biol 23:e3003355
25. Ming G, Song H (2011) Adult Neurogenesis in the Mammalian Brain: Significant Answers and Significant Questions. Neuron 70:687–702
26. Kempermann G, Song H, Gage FH (2015) Neurogenesis in the Adult Hippocampus. Cold Spring Harb Perspect Biol 7:a018812
27. Bonzano S, Crisci I, Podlesny-Drabiniok A, Rolando C, Krezel W, Studer M et al (2018) Neuron-Astroglia Cell Fate Decision in the Adult Mouse Hippocampal Neurogenic Niche Is Cell-Intrinsically Controlled by COUP-TFI In Vivo. Cell Rep 24:329–341
28. Bonzano S, Dallorto E, Molineris I, Michelon F, Crisci I, Gambarotta G et al (2023) NR2F1 shapes mitochondria in the mouse brain, providing new insights into Bosch-Boonstra-Schaaf optic atrophy syndrome. Dis Models Mech 16:dmm049854
29. Bertacchi M, Romano AL, Loubat A, Tran Mau-Them F, Willems M, Faivre L et al (2020) NR2F1 regulates regional progenitor dynamics in the mouse neocortex and cortical gyrification in BBSOAS patients. EMBO J 39:e104163
30. Chen C-A, Wang W, Pedersen SE, Raman A, Seymour ML, Ruiz FR et al (2020) Nr2f1 heterozygous knockout mice recapitulate neurological phenotypes of Bosch-Boonstra-Schaaf optic atrophy syndrome and show impaired hippocampal synaptic plasticity. Hum Mol Genet 29:705–715
31. Maass JG, Kamionek D, Mantilleri A, Theiss S, Dötsch L, Franke F et al (2025) Models of Bosch-Boonstra-Schaaf optic atrophy syndrome reveal genotype-phenotype correlations in brain structure and behavior. Dis Model Mech 18:dmm052426
32. Armentano M, Filosa A, Andolfi G, Studer M (2006) COUP-TFI is required for the formation of commissural projections in the forebrain by regulating axonal growth. Development 133:4151–4162
33. Bertacchi M, Gruart A, Kaimakis P, Allet C, Serra L, Giacobini P et al (2019) Mouse Nr2f1 haploinsufficiency unveils new pathological mechanisms of a human optic atrophy syndrome. EMBO Mol Med 11:e10291
34. Jurkute N, Bertacchi M, Arno G, Tocco C, Kim US, Kruszewski AM et al (2021) Pathogenic NR2F1 variants cause a developmental ocular phenotype recapitulated in a mutant mouse model. Brain Commun 3:fcab162
35. Murai T, Okuda S, Tanaka T, Ohta H (2007) Characteristics of object location memory in mice: Behavioral and pharmacological studies. Physiol Behav 90:116–124
36. Denninger JK, Smith BM, Kirby ED (2018) Novel Object Recognition and Object Location Behavioral Testing in Mice on a Budget. J Vis Exp. 10.3791/58593

37. Hidisoglu E, Kantar-Gok D, Er H, Acun AD, Yargicoglu P (2018) Alterations in spontaneous delta and gamma activity might provide clues to detect changes induced by amyloid-β administration. Eur J Neurosci 47:1013–1023
38. Hidisoglu E, Kantar D, Ozdemir S, Yargicoglu P (2022) Cognitive dysfunctions and spontaneous EEG alterations induced by hippocampal amyloid pathology in rats. Adv Med Sci 67:328–337
39. Crisci I, Bonzano S, Nicolas Z, Dallorto E, Peretto P, Krezel W et al (2024) Tamoxifen exerts direct and microglia-mediated effects preventing neuroinflammatory changes in the adult mouse hippocampal neurogenic niche. Glia 72:1273–1289
40. Savage JT, Ramirez JJ, Risher WC, Wang Y, Irala D, Eroglu C (2024) SynBot is an open-source image analysis software for automated quantification of synapses. Cell Rep Methods 4:100861
41. Hidisoglu E, Chiantia G, Franchino C, Tomagra G, Giustetto M, Carbone E et al (2022) The ryanodine receptor–calstabin interaction stabilizer S107 protects hippocampal neurons from GABAergic synaptic alterations induced by Abeta42 oligomers. J Physiol 600:5295–5309
42. Liu YB, Ye GL, Liu XS, Pasternak JF, Trommer BL (1998) GABAA currents in immature dentate gyrus granule cells. J Neurophysiol 80:2255–2267
43. Zerimech S, Chever O, Scalmani P, Pizzamiglio L, Duprat F, Mantegazza M (2020) Cholinergic modulation inhibits cortical spreading depression in mouse neocortex through activation of muscarinic receptors and decreased excitatory/inhibitory drive. Neuropharmacology 166:107951
44. Russo I, Gavello D, Menna E, Vandael D, Veglia C, Morello N et al (2019) p140Cap Regulates GABAergic Synaptogenesis and Development of Hippocampal Inhibitory Circuits. Cereb Cortex 29:91–105
45. Schneggenburger R, Sakaba T, Neher E (2002) Vesicle pools and short-term synaptic depression: lessons from a large synapse. Trends Neurosci 25:206–212
46. Schneggenburger R, Meyer AC, Neher E (1999) Released fraction and total size of a pool of immediately available transmitter quanta at a calyx synapse. Neuron 23:399–409
47. Baldelli P, Fassio A, Valtorta F, Benfenati F (2007) Lack of synapsin I reduces the readily releasable pool of synaptic vesicles at central inhibitory synapses. J Neurosci 27:13520–13531
48. Stevens CF, Williams JH (2007) Discharge of the Readily Releasable Pool With Action Potentials at Hippocampal Synapses. J Neurophysiol 98:3221–3229
49. Chiantia G, Comai D, Hidisoglu E, Gurgone A, Franchino C, Carabelli V et al (2025) Glyphosate impairs both structure and function of GABAergic synapses in hippocampal neurons. Neuropharmacology 262:110183
50. Forte N, Binda F, Contestabile A, Benfenati F, Baldelli P (2020) Synapsin I Synchronizes GABA Release in Distinct Interneuron Subpopulations. Cereb Cortex 30:1393–1406
51. Aimone JB, Li Y, Lee SW, Clemenson GD, Deng W, Gage FH (2014) Regulation and Function of Adult Neurogenesis: From Genes to Cognition. Physiol Rev 94:991–1026

52. Berron D, Schütze H, Maass A, Cardenas-Blanco A, Kuijf HJ, Kumaran D et al (2016) Strong Evidence for Pattern Separation in Human Dentate Gyrus. J Neurosci 36:7569–7579
53. Assini FL, Duzzioni M, Takahashi RN (2009) Object location memory in mice: Pharmacological validation and further evidence of hippocampal CA1 participation. Behav Brain Res 204:206–211
54. Blackmore DG, Brici D, Walker TL (2022) Protocol for three alternative paradigms to test spatial learning and memory in mice. STAR Protocols 3:101500
55. Vogel-Ciernia A, Wood MA (2014) Examining Object Location and Object Recognition Memory in Mice. Curr Protoc Neurosci. ;69:8.31.1–8.31.17.
56. Deng W, Mayford M, Gage FH (2013) Selection of distinct populations of dentate granule cells in response to inputs as a mechanism for pattern separation in mice. eLife 2:e00312
57. Wilmerding LK, Kondratyev I, Shi WB, Ramirez S, Hasselmo ME (2025) Nonspecific ensemble reactivation in mouse dentate gyrus disrupts spatial working memory. iScience. ;28
58. Yin H, Sun X, Yang K, Lan Y, Lu Z (2025) Regulation of dentate gyrus pattern separation by hilus ectopic granule cells. Cogn Neurodyn 19:10
59. Chiaruttini N, Castoldi C, Requie LM, Camarena-Delgado C, Bianco BD, Gräff J et al (2025) ABBA+BraiAn, an integrated suite for whole-brain mapping, reveals brain-wide differences in immediate-early genes induction upon learning. Cell Rep. ;44
60. Greenberg ME, Ziff EB, Greene LA (1986) Stimulation of Neuronal Acetylcholine Receptors Induces Rapid Gene Transcription. Science 234:80–83
61. Altman J, Das GD (1965) Post-Natal Origin of Microneurones in the Rat Brain. Nature 207:953–956
62. Obernier K, Alvarez-Buylla A (2019) Neural stem cells: origin, heterogeneity and regulation in the adult mammalian brain. Development 146:dev156059
63. Hatami M, Conrad S, Naghsh P, Alvarez-Bolado G, Skutella T (2018) Cell-Biological Requirements for the Generation of Dentate Gyrus Granule Neurons. Front Cell Neurosci. ;12
64. Simon R, Brylka H, Schwegler H, Venkataramanappa S, Andratschke J, Wiegreffe C et al (2012) A dual function of Bcl11b/Ctip2 in hippocampal neurogenesis. EMBO J 31:2922–2936
65. Steiner B, Klempin F, Wang L, Kott M, Kettenmann H, Kempermann G (2006) Type-2 cells as link between glial and neuronal lineage in adult hippocampal neurogenesis. Glia 54:805–814
66. Chaudhry FA, Reimer RJ, Bellocchio EE, Danbolt NC, Osen KK, Edwards RH et al (1998) The Vesicular GABA Transporter, VGAT, Localizes to Synaptic Vesicles in Sets of Glycinergic as Well as GABAergic Neurons. J Neurosci 18:9733–9750
67. Choii G, Ko J (2015) Gephyrin: a central GABAergic synapse organizer. Exp Mol Med 47:e158
68. Hosp JA, Strüber M, Yanagawa Y, Obata K, Vida I, Jonas P et al (2014) Morpho-physiological criteria divide dentate gyrus interneurons into classes. Hippocampus 24:189–203
69. Kepecs A, Fishell G (2014) Interneuron cell types are fit to function. Nature 505:318–326
70. Groisman AI, Yang SM, Schinder AF (2020) Differential Coupling of Adult-Born Granule Cells to Parvalbumin and Somatostatin Interneurons. Cell Rep 30:202–214e4

71. Espinoza C, Guzman SJ, Zhang X, Jonas P (2018) Parvalbumin+ interneurons obey unique connectivity rules and establish a powerful lateral-inhibition microcircuit in dentate gyrus. Nat Commun 9:4605
72. Medrihan L, Ferrea E, Greco B, Baldelli P, Benfenati F (2015) Asynchronous GABA Release Is a Key Determinant of Tonic Inhibition and Controls Neuronal Excitability: A Study in the Synapsin II-/- Mouse. Cereb Cortex 25:3356–3368
73. Marcantoni A, Cerullo MS, Buxeda P, Tomagra G, Giustetto M, Chiantia G et al (2020) Amyloid Beta42 oligomers up-regulate the excitatory synapses by potentiating presynaptic release while impairing postsynaptic NMDA receptors. J Physiol 598:2183–2197
74. GoodSmith D, Kim SH, Puliyadi V, Ming G, Song H, Knierim JJ et al (2022) Flexible encoding of objects and space in single cells of the dentate gyrus. Curr Biol 32:1088–1101e5
75. Kitchigina VF, Shubina LV, Popova IY (2022) The Role of the Dentate Gyrus in Mediating Hippocampal Functions: The Healthy Brain. Neurosci Behav Physi 52:1401–1417
76. Borzello M, Ramirez S, Treves A, Lee I, Scharfman H, Stark C et al (2023) Assessments of dentate gyrus function: discoveries and debates. Nat Rev Neurosci 24:502–517
77. Martin L, Sample H, Gregg M, Wood C (2014) Validation of operant social motivation paradigms using BTBR T + tf/J and C57BL/6J inbred mouse strains. Brain Behav 4:754–764
78. Kazdoba TM, Leach PT, Crawley JN (2016) Behavioral phenotypes of genetic mouse models of autism. Genes Brain Behav 15:7–26
79. Xia Q, Walker AK, Song C, Wang J, Singh A, Mobley JA et al (2023) Effects of heterozygous deletion of autism-related gene Cullin-3 in mice. PLoS ONE 18:e0283299
80. Pelkey KA, Chittajallu R, Craig MT, Tricoire L, Wester JC, McBain CJ (2017) Hippocampal GABAergic Inhibitory Interneurons. Physiol Rev 97:1619–1747
81. Lee C-T, Kao M-H, Hou W-H, Wei Y-T, Chen C-L, Lien C-C (2016) Causal Evidence for the Role of Specific GABAergic Interneuron Types in Entorhinal Recruitment of Dentate Granule Cells. Sci Rep 6:36885
82. Hu H, Gan J, Jonas P, Fast-spiking (2014) parvalbumin+ GABAergic interneurons: From cellular design to microcircuit function. Science 345:1255263
83. Lee S-H, Kang Y-J, Smith BN Activation of hypoactive parvalbumin-positive fast-spiking interneuron restores dentate inhibition to prevent epileptiform activity in the mouse intrahippocampal kainate model of temporal lobe epilepsy. bioRxiv. 2024:2024.04.05.588316.
84. Wöhr M, Orduz D, Gregory P, Moreno H, Khan U, Vörckel KJ et al (2015) Lack of parvalbumin in mice leads to behavioral deficits relevant to all human autism core symptoms and related neural morphofunctional abnormalities. Transl Psychiatry 5:e525
85. Wirk E, Quairiaux C, Marissal T (2025) Parvalbumin interneurons: the dark and bright sides of a key playmaker of neural circuits and behavior. Front Cell Neurosci. ;19

86. Tripodi M, Filosa A, Armentano M, Studer M (2004) The COUP-TF nuclear receptors regulate cell migration in the mammalian basal forebrain. Development 131:6119–6129
87. Hu JS, Vogt D, Lindtner S, Sandberg M, Silberberg SN, Rubenstein JLR (2017) Coup-TF1 and Coup-TF2 control subtype and laminar identity of MGE-derived neocortical interneurons. Development 144:2837–2851
88. Rech ME, McCarthy JM, Chen C-A, Edmond JC, Shah VS, Bosch DGM et al (2020) Phenotypic expansion of Bosch–Boonstra–Schaaf optic atrophy syndrome and further evidence for genotype–phenotype correlations. Am J Med Genet Part A 182:1426–1437
89. Hefft S, Jonas P (2005) Asynchronous GABA release generates long-lasting inhibition at a hippocampal interneuron-principal neuron synapse. Nat Neurosci 8:1319–1328
90. Hagler DJ, Goda Y (2001) Properties of Synchronous and Asynchronous Release During Pulse Train Depression in Cultured Hippocampal Neurons. J Neurophysiol 85:2324–2334
91. Kaeser PS, Regehr WG (2014) Molecular mechanisms for synchronous, asynchronous, and spontaneous neurotransmitter release. Annu Rev Physiol 76:333–363
92. Rozov A, Bolshakov AP, Valiullina-Rakhmatullina F (2019) The Ever-Growing Puzzle of Asynchronous Release. Front Cell Neurosci 13:28
93. Chanaday NL, Kavalali ET (2018) Presynaptic origins of distinct modes of neurotransmitter release. Curr Opin Neurobiol 51:119–126
94. Malagon G, Myeong J, Klyachko VA (2023) Two forms of asynchronous release with distinctive spatiotemporal dynamics in central synapses. eLife 12:e84041
95. Sun J, Pang ZP, Qin D, Fahim AT, Adachi R, Südhof TC (2007) A dual-Ca2+-sensor model for neurotransmitter release in a central synapse. Nature 450:676–682
96. Jackman SL, Regehr WG (2017) The Mechanisms and Functions of Synaptic Facilitation. Neuron 94:447–464
97. Simbürger E, Plaschke M, Kirsch J, Nitsch R (2000) Distribution of the receptor-anchoring protein gephyrin in the rat dentate gyrus and changes following entorhinal cortex lesion. Cereb Cortex 10:422–432
98. Tretter V, Mukherjee J, Maric H-M, Schindelin H, Sieghart W, Moss SJ (2012) Gephyrin, the enigmatic organizer at GABAergic synapses. Front Cell Neurosci 6:23

Figures

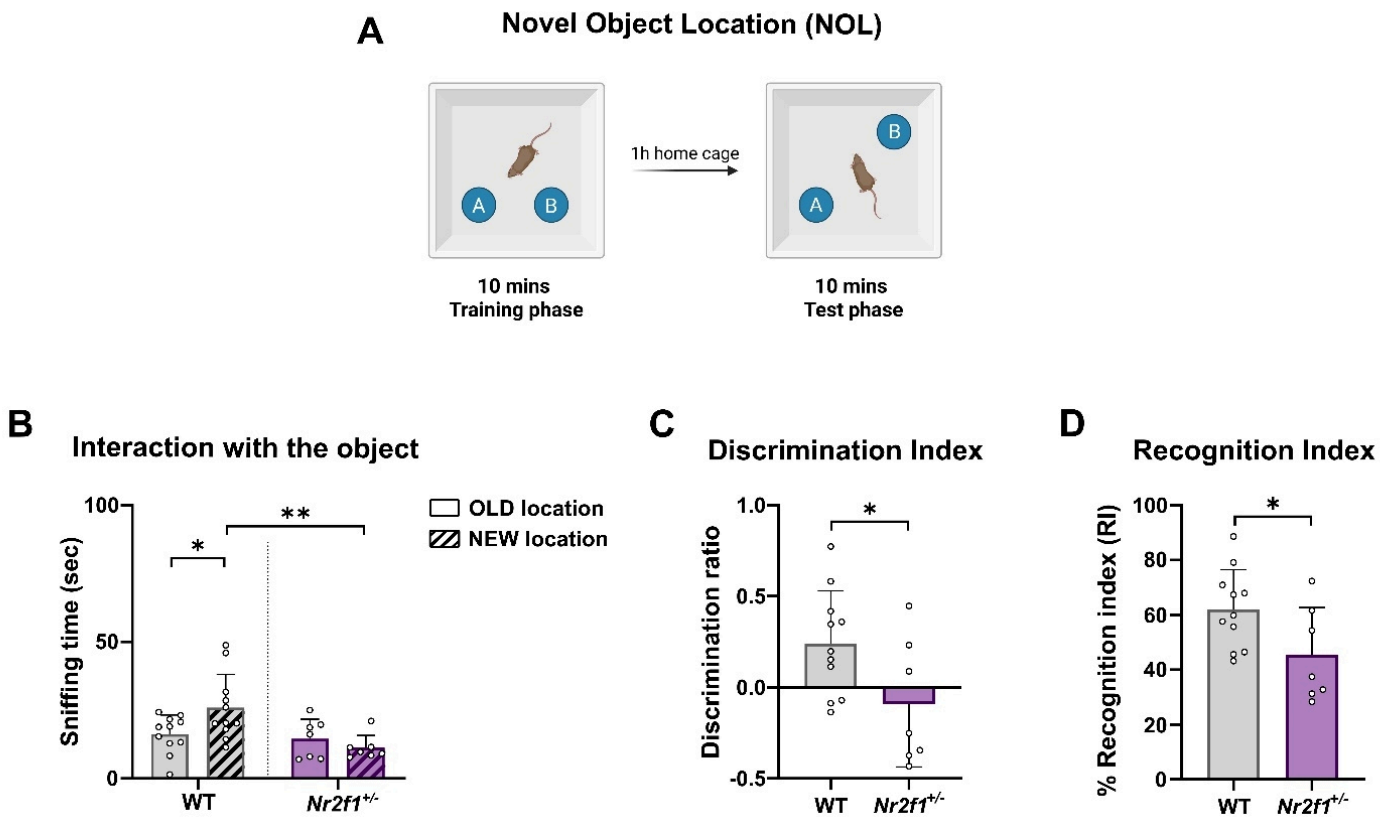


Figure 1

Impaired short-term spatial memory in adult *Nr2f1*$^{+/-}$ mice (A) Schematic representation of the Novel Object Location (NOL) behavioral test. **(B)** Bar dot plots showing the quantification of object exploration time (i.e. sniffing time in seconds) during the test phase in WT (grey) and *Nr2f1*$^{+/-}$ (purple) mice. Striped bars indicate the interaction time with the object placed in the novel location. Two-tailed unpaired Student's t-test, old versus new location WT: **p*=0.0320, *Nr2f1*$^{+/-}$: n.s. Mann-Whitney test for WT versus *Nr2f1*$^{+/-}$ in the new location ***p*=0.0028. **(C,D)** Bar plots showing the exploration preference of *Nr2f1*$^{+/-}$ mice (purple) versus WT (grey) by using the standardized discrimination (Two-tailed unpaired Student's t-test, **p*=0.0419) and recognition indexes (Two-tailed unpaired Student's t-test, **p*=0.0419). Each dot represents an animal (n = 11 WT / 7 *Nr2f1*$^{+/-}$ mice). Error bars indicate mean± SD.

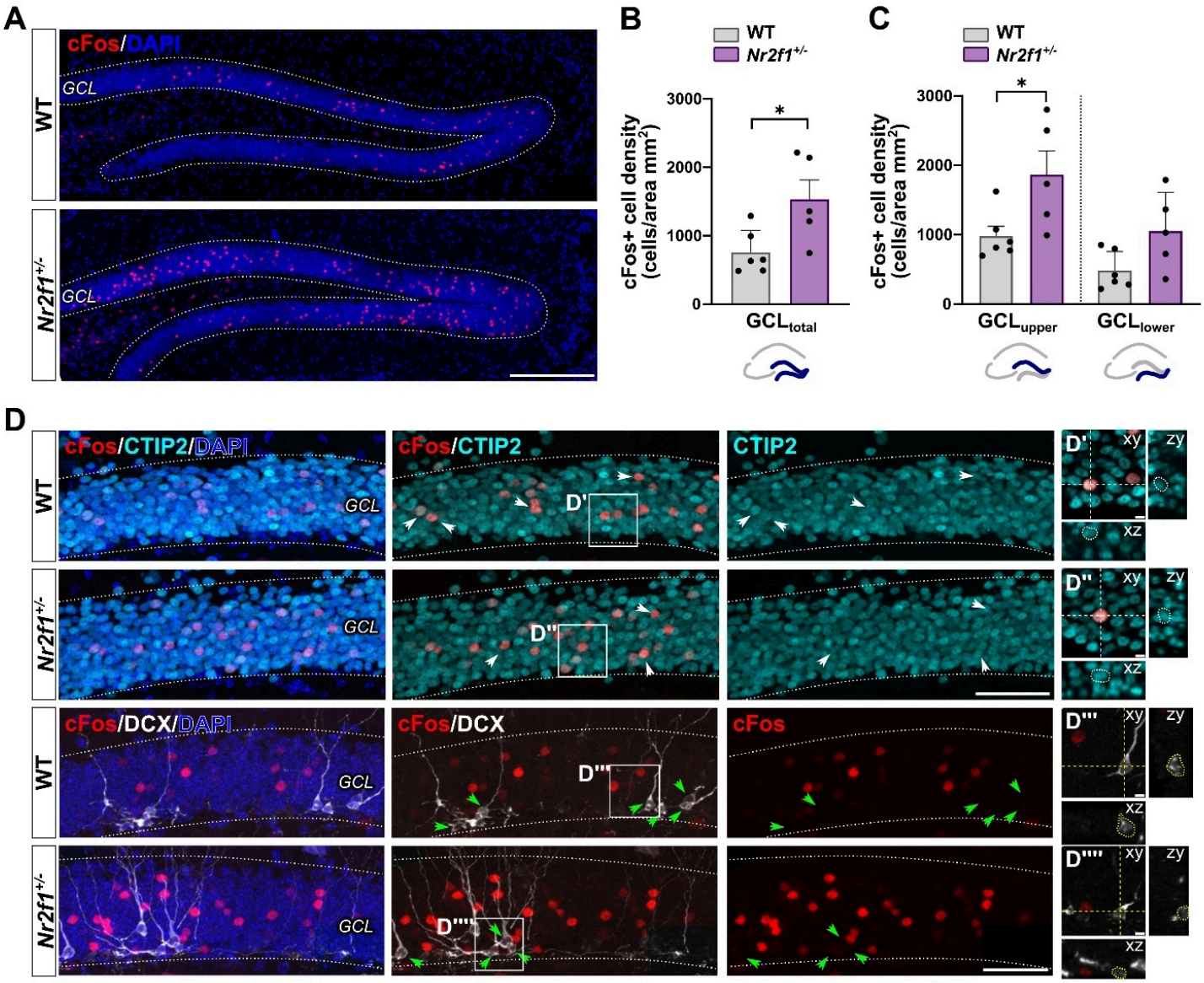


Figure 2

Increased cFos expression in DG granule neurons of *Nr2f1*$^{+/-}$ mice (A) Representative confocal images of the granule cell layer (GCL) of the dentate gyrus (DG) immunostained for cFos (red) and DAPI (blue) in WT and *Nr2f1*$^{+/-}$ mice. Dashed lines outline the GCL. **(B-C)** Quantification of cFos-positive cell density (cells/mm^2) in the whole GCL (two-tailed unpaired Student's t-test, *p=0.0261) **(B)** and separately in the upper (left) (two-tailed unpaired Student's t-test, *p=0.0317) and lower (right) blades of the DG (two-tailed unpaired Student's t-test, p=0.0528) **(C)** in adult WT (grey) and *Nr2f1*$^{+/-}$ (purple) mice. Each dot represents one animal (n = 6 WT / 5 *Nr2f1*$^{+/-}$mice). Error bars indicate mean± SD. **(D)** Representative high-magnification confocal images of the upper GCL stained for cFos (red), CTIP2 (cyan), DCX (white), and DAPI (blue) in WT and *Nr2f1*$^{+/-}$ mice. White arrowheads indicate double positive cFos$^+$/CTIP2$^+$ cells, whereas green arrowheads indicate DCX$^+$ cells lacking cFos expression. **(D'–D'''')** Zoomed-in views and orthogonal projections (xy, xz, zy) highlight co-localization of cFos with CTIP2 **(D', D'')** and absence of cFos expression in DCX$^+$ selected cells **(D''', D'''')**.

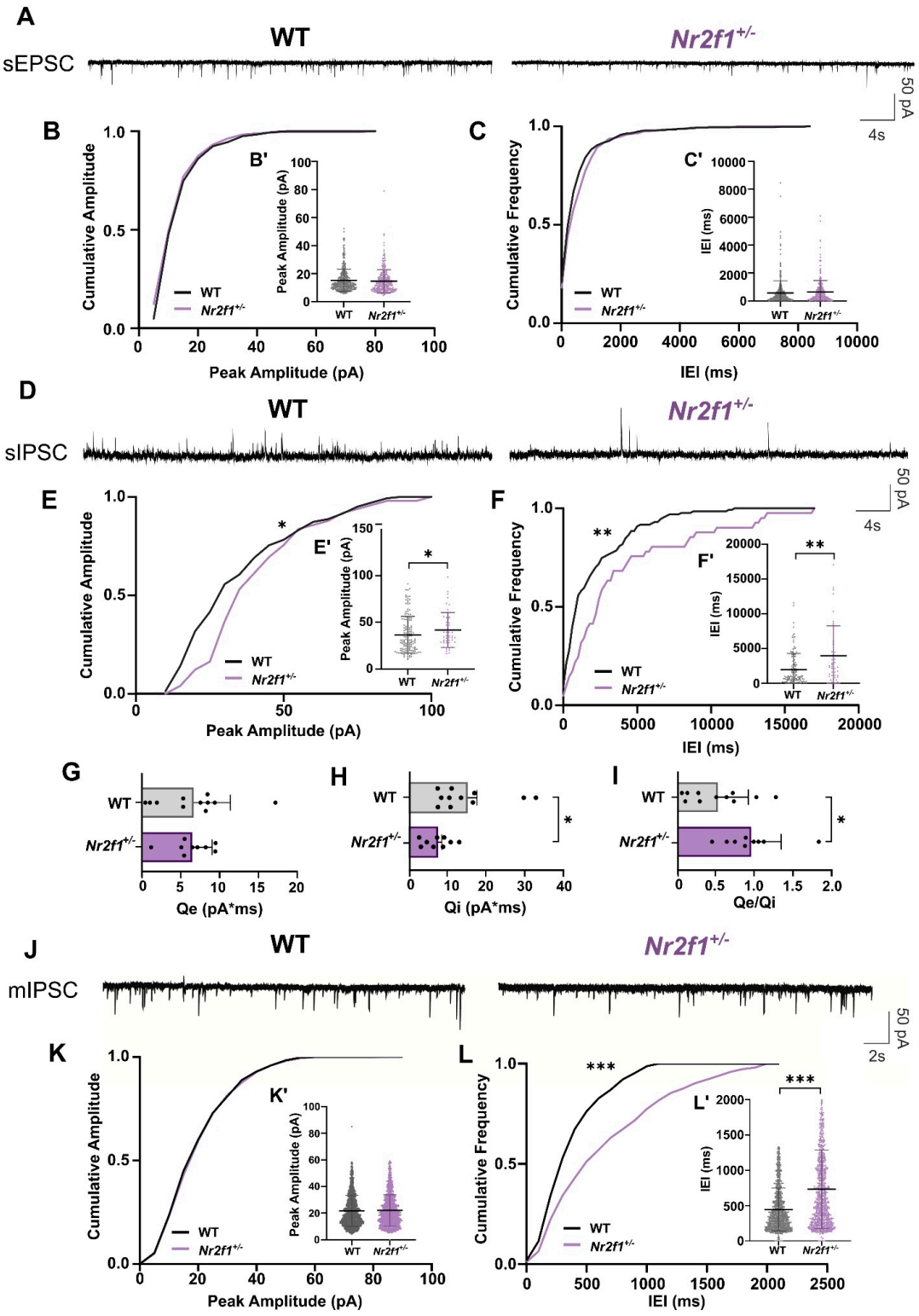


Figure 3

Spontaneous and miniature synaptic transmission in DG granule cells from adult WT and *Nr2f1*$^{+/-}$ mice. **(A, D)** Representative traces of spontaneous excitatory and inhibitory postsynaptic currents, respectively, recorded from DG granule neurons in acute hippocampal slices from adult WT and *Nr2f1*$^{+/-}$ mice. Recordings were obtained from WT (n = 11 cells) and *Nr2f1*$^{+/-}$ *mice* (n = 9 cells). **(B)** Cumulative

probability distribution of sEPSC peak amplitudes in WT (black line) and *Nr2f1*$^{+/-}$ (purple line) GCs, showing no significant difference between genotypes (Kolmogorov-Smirnov test, p=0.06). **(B')** Scatter plot representing sEPSC peak amplitudes for all recorded cells. (WT: 15.21 ± 7.88 pA vs *Nr2f1*$^{+/-}$: 15.03 ± 8.44 pA, Mann-Whitney test, p= 0.51). **(C)** Cumulative probability distribution of sEPSC inter-event intervals in WT and *Nr2f1*$^{+/-}$GCs, showing no significant difference between genotypes (Kolmogorov-Smirnov test, p=0.06). **(C')** Scatter plot of sEPSC inter-event intervals for all detected events. (WT: 572.4 ± 872.9 ms vs. *Nr2f1*$^{+/-}$: 642.3 ± 822.8, Mann-Whitney test, p= 0.052). **(E)** Cumulative probability distribution of sIPSC peak amplitudes in WT and *Nr2f1*$^{+/-}$GCs, showing a rightward shift in *Nr2f1*$^{+/-}$ neurons, consistent with increased inhibitory event amplitude (WT: 36.56 ± 19.73 pA vs. 41.72 ± 18.65 pA, Kolmogorov-Smirnov test, *p= 0.011). **(E')** Scatter plot representing sIPSC peak amplitudes for individual cells (Mann-Whitney test, *p= 0.03). **(F)** Cumulative probability distribution of sIPSC inter-event intervals in WT and *Nr2f1*$^{+/-}$ GCs, showing a leftward shift in *Nr2f1*$^{+/-}$ neurons, consistent with increased inhibitory event frequency. (1991 ± 2316 ms vs. *Nr2f1*$^{+/-}$: 3955 ± 4314 ms, Kolmogorov-Smirnov test, **p=0.004). **(F')** Scatter plot showing sIPSC inter-event intervals for all detected events (Mann-Whitney test, **p= 0.002). **(G)** Scatter plot showing no significant difference in excitatory charge transfer between WT and *Nr2f1*$^{+/-}$ GCs. (WT: 6.50 ± 4.70 pC vs. *Nr2f1*$^{+/-}$: 6.28 ± 2.57 pC, Student's t test, p=0.90). **(H)** Scatter plot showing reduced inhibitory charge transfer in *Nr2f1*$^{+/-}$ GCs (WT: 14.75 ± 8.65 pC vs. *Nr2f1*$^{+/-}$: 7.09 ± 3.49 pC, Student's t test, *p=0.02). **(I)** Scatter plot showing the excitatory/inhibitory balance, expressed as the Qe/Qi ratio, in WT and *Nr2f1*$^{+/-}$ GCs (WT: 0.51 ± 0.40 vs. *Nr2f1*$^{+/-}$: 0.95 ±0.40, Student's t test, *p=0.03). **(J)** Representative traces of miniature inhibitory postsynaptic currents (mIPSCs) recorded from DG granule neurons in acute hippocampal slices from adult WT (n=23 cells) and *Nr2f1*$^{+/-}$ mice (n=28 cells). **(K)** Cumulative probability distribution of mIPSC peak amplitudes in WT (black line) and *Nr2f1*$^{+/-}$ (purple line) granule neurons, showing no significant difference between groups (WT: 21.78 ± 11.71 pA vs. *Nr2f1*$^{+/-}$: 22.02 ± 11.75 pA; Kolmogorov–Smirnov test, p = 0.1694). **(K')** Scatter plot showing distribution of mIPSCs peak amplitudes from WT (dark grey) and *Nr2f1*$^{+/-}$ (purple) granule neurons. **(L)** Cumulative probability distribution of inter-event intervals (IEIs) of mIPSCs in WT (black line) and *Nr2f1*$^{+/-}$ (purple line) granule neurons, revealing a significant rightward shift toward longer interevent intervals in granule neurons of *Nr2f1*$^{+/-}$ (WT: 400.8 ± 250.8 ms vs. *Nr2f1*$^{+/-}$: 683.5 ± 497.2 ms, Kolmogorov–Smirnov test, p < 0.0001). **(L')** Scatter plot showing IEIs distribution of all detected mIPSC events recorded from WT (dark grey) and *Nr2f1*$^{+/-}$ (purple) granule neurons. Error bars indicate mean± SD.

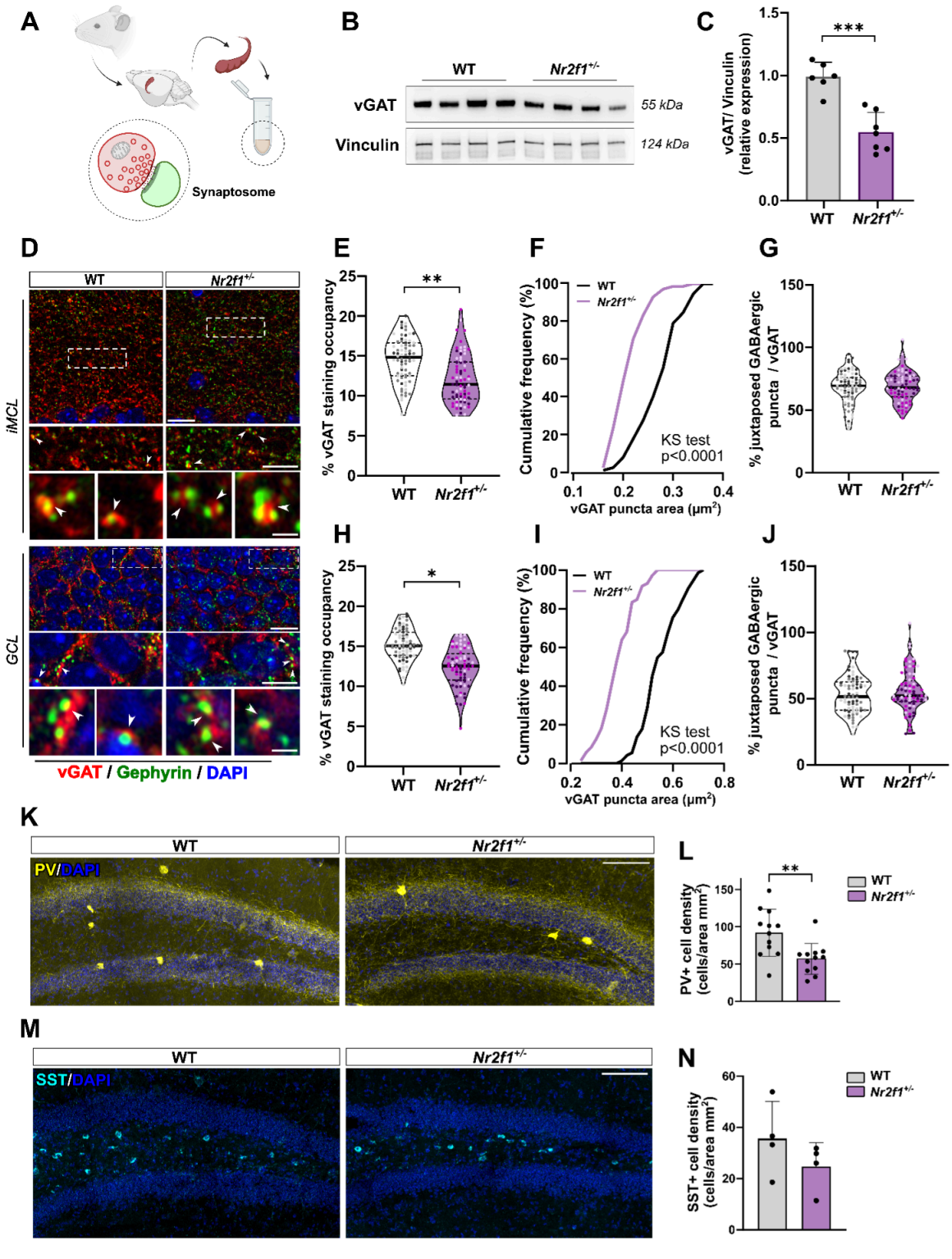


Figure 4

Reduced presynaptic vGAT levels and reduced density of PV+ interneurons in the DG of adult *Nr2f1*$^{+/-}$ mice (A) Schematic representation of the synaptosome extraction protocol from fresh adult hippocampi. **(B)** Representative Western blot of isolated synaptosomal proteins from WT and Nr*2f1*$^{+/-}$ hippocampi, probed for vesicular GABA transporter (vGAT; 55 kDa) and vinculin (124 kDa). **(C)** Quantification of vGAT protein levels normalized to vinculin and expressed relative to WT samples. Each dot represents one

animal (n = 6 WT/ 7 *Nr2f1*$^{+/-}$). Error bars indicate mean± SD. Two-tailed unpaired Student's t-test, **p*=0.0167. **(D)** Representative confocal images of inner molecular (iMCL) and granule cell layers (GCL) immunostained for vGAT (red), gephyrin (green), and DAPI (blue) in WT and *Nr2f1*$^{+/-}$ mice. Insets show higher magnification views. White arrowheads indicate juxtaposed puncta. Scale bars: 10µm, 5µm, 1µm. **(E–G)** Quantitative analysis of vGAT staining in the iMCL. **(E)** Violin plot showing presynaptic vGAT occupancy (fractional area) in WT (white) and *Nr2f1*$^{+/-}$ (purple) mice (Two-tailed nested t-test ***p*=0.0083). Each dot represents one region of interest (ROI). Three animals per genotype were analyzed (n = 3 WT/ *Nr2f1*$^{+/-}$mice), with ROIs color-coded by animal. Error bars indicate median ± SD **(F)** Cumulative frequency distribution of the vGAT puncta area in WT (white) and *Nr2f1*$^{+/-}$ (purple) mice (Kolmogorov–Smirnov test, *p*<0.0001; n = 72 ROIs per genotype). **(G)** Violin plot showing the percentage of vGAT-positive puncta juxtaposed to gephyrin-positive puncta, over the total number of vGAT-positive puncta WT (white) and *Nr2f1*$^{+/-}$ (purple) mice (Two-tailed nested t-test, n.s.). Three animals per genotype were analyzed (n = 3 WT/ *Nr2f1*$^{+/-}$), with ROIs color-coded by animal. Error bars indicate median ± SD. **(H–J)** Quantitative analysis of vGAT staining in the GCL. **(H)** Violin plot showing vGAT occupancy (fractional area) in WT (white) and *Nr2f1*$^{+/-}$(purple) mice (two-tailed nested t-test **p*=0.0434). Each dot represents a selected region of interest (ROI). Three animals per genotype were analyzed (n = 3 WT/ *Nr2f1*$^{+/-}$), with ROIs color-coded by animal. Error bars indicate median ± SD. **(I)** Cumulative frequency distribution of vGAT puncta area in WT (white) and *Nr2f1*$^{+/-}$(purple) mice (Kolmogorov–Smirnov test, *p*<0.0001; *n* = 72 ROIs per genotype). **(J)** Violin plot showing percentage of vGAT-gephyrin juxtaposed puncta over the total number of vGAT-positive puncta in the GCL of WT (white) and *Nr2f1*$^{+/-}$ (purple) mice (two-tailed nested t-test, n.s.). Three animals per genotype were analyzed (n = 3 WT/ *Nr2f1*$^{+/-}$mice), with ROIs color-coded by animal. Error bars indicate median ± SD. **(K,M)** Representative confocal images of parvalbumin (PV) (yellow) (A) and somatostatin (SST) (C) immunofluorescence staining in the DG of WT and *Nr2f1*$^{+/-}$ mice. Nuclei are counterstained with DAPI (blue). Scalebars 100 µm. **(L,N)** Bar plots showing the quantification of PV+ (B) and SST+ (D) interneuron density (cells/mm^2) in the GCL of WT (grey) and *Nr2f1*$^{+/-}$ (purple) mice. PV+ cell density was reduced in *Nr2f1*$^{+/-}$ (Two-tailed unpaired Student's t-test, ***p*=0.0037), whereas SST+ cell density was unchanged (Two-tailed unpaired Student's t-test, p=0.2546). Each dot represents one animal (PV: n = 12 WT / 12 *Nr2f1*$^{+/-}$mice; SST: n = 4 WT / 4 *Nr2f1*$^{+/-}$ mice). Error bars indicate mean± SD.

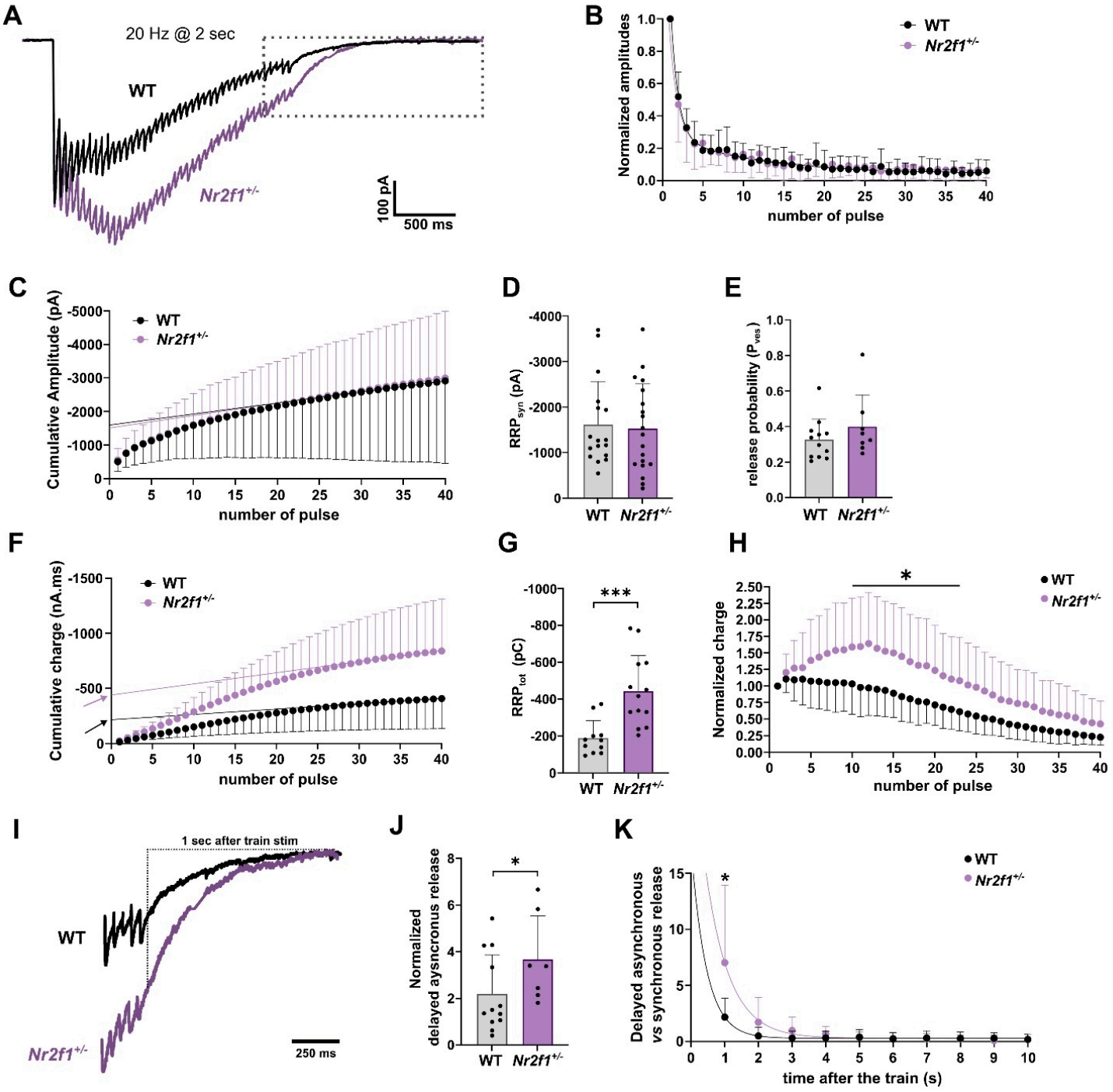


Figure 5

DG GABAergic terminals of *Nr2f1*$^{+/-}$ mice exhibit enhanced asynchronous release, while synchronous release remains unaffected (A) Representative eIPSC traces recorded during 20 Hz stimulation train (2 s) in DG granule neurons from WT (black, n=17 cells) and *Nr2f1*$^{+/-}$ (purple, n=19 cells) mice. **(B)** Time course of the normalized eIPSC amplitude (means ± SD) versus time during 20 Hz train stimulation for 2s. No differences between WT (black) and *Nr2f1*$^{+/-}$ (purple) granule neurons have been observed. **(C)** Cumulative eIPSC amplitude as a function of the number of pulses during 20 Hz train in granule neurons

of WT (black) and *Nr2f1*$^{+/-}$ (purple). The size of RRP_{syn} was determined by fitting data points within the range of the 30th to 40th stimuli using linear regression, and then back-extrapolated to time zero to estimate the cumulative eIPSC amplitude before steady-state depression. **(D)** The size of RRP_{syn} is shown as mean ± SD in granule neurons of WT (grey) and *Nr2f1*$^{+/-}$ (purple) mice (WT: 1600.0 ± 947.3 pA vs. *Nr2f1*$^{+/-}$: 1511.0 ± 986.1 pA; n = 17 and 19 cells, respectively; p=0.7865, unpaired Student's t-test,). **(E)** Bar graph showing the average release probability value (P_{ves}), in granule neurons of WT (grey) and *Nr2f1*$^{+/-}$ (purple) neurons (WT: 0.32 ± 0.12, n = 12 vs. *Nr2f1*$^{+/-}$: 0.40 ± 0.18, n = 8; p= 0.3054, Mann-Whitney test). **(F)** Cumulative eIPSC charge measured during 20 Hz stimulation (2 s) in granule neurons of WT (black) and *Nr2f1*$^{+/-}$ (purple) mice. The intercept between the linear fit and y-axes gives an estimation of the total RRP (RRP_{tot}), indicated by arrows. **(G)** Bar graph comparing the average RRP_{tot} size in WT (grey) and *Nr2f1*$^{+/-}$ (purple) neurons (WT: -186.7 ± 94.2 pC vs. *Nr2f1*$^{+/-}$: -440.4 ± 192.7 pC; n = 11 and 13 cells, respectively; ***p=0.0003, Mann-Whitney test). **(H)** Time course of the normalized eIPSC area (means ± SD) versus time during 20 Hz train stimulation for 2 s WT (black) and *Nr2f1*$^{+/-}$ (purple) neurons. **(I)** Last part of the traces in (A) shown at higher magnitude. The area below the traces (dashed lines) corresponds to the first second of asynchronous release after the end of 20 Hz evoked current. This area was considered for measuring the delayed asynchronous release. **(J)** Bar graph comparing the amount of delayed asynchronous response normalized vs. the synchronous release in granule neurons of WT (grey) and *Nr2f1*$^{+/-}$ (purple) mice during 1 s after the end to the train. In WT it was 2.16 ± 1.68 times higher than synchronous release while in *Nr2f1*$^{+/-}$ it was 3.64 ± 1.87 time higher than synchronous release; n = 12 and 7 cells, respectively; *p=0.0449, Mann–Whitney test. **(K)** The time course of asynchronous charge during 10 s following the end of the train stimulation. As shown in **J**, asynchronous release during the first second is significantly higher in granule neurons of *Nr2f1*$^{+/-}$ (purple) compared to WT (black) mice (*p<0.05). Data are presented as mean ± SD.

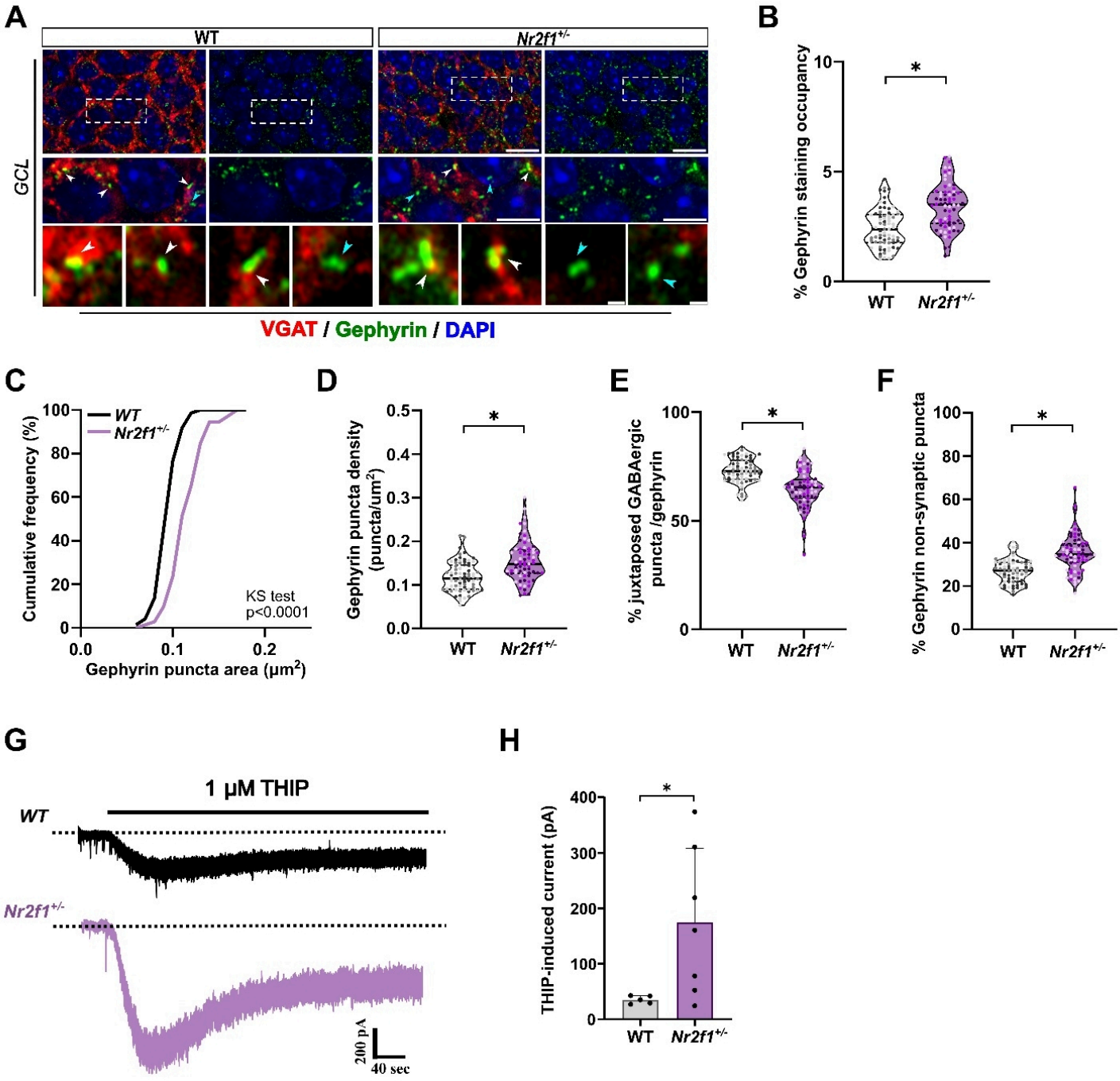


Figure 6

Altered gephyrin distribution and increased THIP-induced tonic inhibition in the adult DG of *Nr2f1*$^{+/-}$ mice. **(A)** Representative confocal images of the DG granule cell layer (GCL) immunostained for vGAT (red), gephyrin (green), and DAPI (blue) in WT and *Nr2f1*$^{+/-}$ mice. Insets show magnified views. White arrowheads indicate juxtaposed puncta; cyan arrowheads indicate non-juxtaposed gephyrin puncta. Scale bars 10µm, 5µm, 0.5µm. **(B–F)** Quantitative analysis of gephyrin staining in the GCL. **(B)** Violin plot showing gephyrin occupancy expressed as the percentage of the area occupied by gephyrin immunofluorescence signal in the GCL of WT (white) and *Nr2f1*$^{+/-}$ (purple) mice (Two-tailed nested t-test *p=0.0416). Each dot represents a selected region of interest (ROI). Three animals per genotype were

analyzed (n = 3 WT/ *Nr2f1*$^{+/-}$mice), with ROIs from individual animals are color-coded. Error bars indicate median ± SD. **(C)** Cumulative frequency distribution of the gephyrin puncta area in the GCL of WT (white) and *Nr2f1*$^{+/-}$ (purple) mice (Kolmogorov–Smirnov test, $p<0.0001$; n = 72 ROIs per genotype). **(D)** Violin plot showing gephyrin puncta density (puncta/μm^2) in the GCL of WT (white) and *Nr2f1*$^{+/-}$ (purple) mice (Two-tailed nested t-test *p=0.0434). **(E)** Violin plot showing the percentage of gephyrin-positive puncta juxtaposed with vGAT-positive presynaptic terminals relative to total gephyrin puncta in the GCL of WT (white) and *Nr2f1*$^{+/-}$ (purple) mice (Two-tailed nested t-test, *p=0.0365). **(F)** Violin plot representing the percentage of non-juxtaposed (extrasynaptic) gephyrin puncta in the GCL of WT (white) and *Nr2f1*$^{+/-}$ (purple) mice (Two-tailed nested t-test, *p=0.0365). **(B, D-F)** Three animals per genotype were analyzed (n = 3 WT/ *Nr2f1*$^{+/-}$mice), with ROIs from individual animals color-coded. Error bars indicate median ± SD. **(G)** Representative traces showing tonic current responses to 1 μM THIP (gaboxadol), a δ-subunit-containing $GABA_A$ receptor agonist, in DG granule neurons of WT (black, n=5 cells) and *Nr2f1*$^{+/-}$ (purple, n = 7 cells) mice. **(H)** Quantification of THIP-induced tonic current in granule neurons of WT (black, 35.18 ± 7.16 pA, n = 5) and *Nr2f1*$^{+/-}$ (purple, 174.2 ± 133.7 pA, n = 7) mice. Data are presented as mean ± SD (*p=0.048, Mann-Whitney test).

Supplementary Files

This is a list of supplementary files associated with this preprint. Click to download.

- SupplementaryInformationActaNeuropatholCommun.pdf
- SupplementaryinformationUncroppedGelsandBlots10102026.docx